International Journal of Biological Macromolecules 334 (2025) 149092

Contents lists available at ScienceDirect

International Journal of Biological Macromolecules

journal homepage: www.elsevier.com/locate/ijbiomac

Bio-capped ZnO nanoparticles formulated from *Prosopis juliflora gum*: Phytochemical characterization and therapeutic potential

Naveen Thanjavur [a,b], Buddolla Anantha Lakshmi [a,b], Laxmi Bugude [c], Kandaswamy Theyagarajan [a,b], Young-Joon Kim [a,b,*]

[a] *Department of Electronic Engineering, Gachon University, Seongnam, 13120, Republic of Korea*
[b] *Department of Semiconductor Engineering, Gachon University, Seongnam, 13120, Republic of Korea*
[c] *Dr. Buddolla's Institute of Life Sciences, Tirupati, 517506, India*

ARTICLE INFO

Keywords:
Green synthesis
Plant gum
Zinc oxide nanoparticles
Antibacterial activity
Antioxidant properties
Phytochemical-mediated nanotechnology

ABSTRACT

Growing recognition of the phytochemical diversity and therapeutic value of plant-derived materials has driven efforts toward their sustainable use in nanotechnology and biomedical research. Here, we synthesized bio-capped zinc oxide nanoparticles (G-ZnO) using *Prosopis juliflora* gum (PJ-Gum) and evaluated their potential in diverse biomedical applications. LC-QTOF-MS profiling of PJ-Gum confirmed the presence of multiple polyphenols and flavonoid with notable therapeutic relevance. This phytochemical-rich exudate served as both reducing and stabilizing agent during G-ZnO synthesis. The synthesized G-ZnO was characterized using FTIR, UV–Vis, XRD, XPS, zeta potential, SEM, TEM, and DLS analyses, confirming the formation of crystalline nanoparticles with an average size of 34.1 nm and good colloidal stability (−27 mV). Biological assays revealed significant antimicrobial activity against Gram-positive, Gram-negative bacteria and fungal pathogens. Compared to PJ-Gum, G-ZnO exhibited enhanced zones of inhibition, 8.8 ± 0.20 mm for *B. subtilis* and 8.9 ± 0.12 mm for *P. aeruginosa* relative to the control. Further, antioxidant analyses (DPPH and H_2O_2 scavenging assays) demonstrated strong free-radical scavenging potential, while cytocompatibility studies showed >85% cell viability, indicating biosafety for potential biomedical use. Additional in vitro assays suggested notable antidiabetic and anti-inflammatory activities, reinforcing the multifunctional therapeutic potential of G-ZnO. Interestingly, the formation of ZnO nanostructures using PJ-Gum enhanced the inherent biological activities of the PJ-Gum, leading to improved overall bioefficacy. This study highlights PJ-Gum as an efficient phytochemical resource for the green synthesis of G-ZnO nanoparticles exhibiting broad-spectrum bioactivities, including antimicrobial, antioxidant, and therapeutic properties, underscoring their promise for biomedical and pharmaceutical applications.

1. Introduction

The expanding phytochemical diversity and therapeutic value of plant-derived materials have drawn significant scientific interest owing to their effectiveness for treating various illnesses and diseases [1]. According to the World Health Organization, approximately 1.9 million people prefer traditional medicines to avoid the potential side effects of allopathic treatments, reduce costs, and enhance therapeutic effectiveness. This is particularly evident in non-industrialized societies, where up to 80% of the population continues to rely on traditional medicines [2]. Recently, the development of effective plant-derived medicines such as Crofelemer, NexoBird, and the QS-21 adjuvant vaccine has provided alternative therapeutic options for various diseases, including HIV/AIDS, burn wound treatment, and vaccine-based immune enhancement, respectively [3–5]. Notably, numerous potent medicinal properties are derived from rare and seasonal plants; nevertheless, large-scale development remains challenging due to limited availability, inadequate standardization, instability, laborious preparation methods, and slow therapeutic response [6]. To address these limitations, abundantly available plant-based and plant-derived materials such as gums, barks, and roots have been identified, isolated, and functionalized with nanomaterials and other bioactive compounds. These materials have been employed to develop advanced formulations with promising pharmaceutical, biomedical, and industrial applications, including drug delivery systems, drug formulations, controlled release mechanisms, wound dressings, antimicrobial coatings, and food preservatives [7–9].

* Corresponding authors.
E-mail address: youngkim@gachon.ac.kr (Y.-J. Kim).

https://doi.org/10.1016/j.ijbiomac.2025.149092
Received 9 July 2025; Received in revised form 13 November 2025; Accepted 15 November 2025
Available online 17 November 2025

Among various plant derived materials, plant gums have been extensively explored in traditional medicine due to their ease of availability, excellent therapeutic efficacy, and non-toxic nature. Plant gums are naturally occurring complex polysaccharide mixtures obtained from plant exudates, seeds and bark [10]. They exhibit biocompatible, biodegradable, and polymer characteristics, along with a hydrophilic nature and strong film-forming ability, all of which contribute to their significant biomedical potential [11]. Moreover, these gums are rich in secondary metabolites, such as terpenoids, sterols, flavonoids, and polyphenols, including p-hydroxybenzoic acid, which is associated with potent antimicrobial activity. Consequently, plant gums demonstrate a wide spectrum of biological activities, supporting their application in therapeutic formulations such as antimicrobial, antioxidant, anti-inflammatory, digestive, wound healing, drug-delivery, and tissue engineering systems [12,13]. Several gums including Arabic, Tragacanth, Guar, Karaya, and Xanthan have been widely investigated in medical and experimental research [14]. These renewable and eco-friendly biopolymers offer a sustainable alternative to synthetic polymers, effectively bridging traditional herbal medicine with modern therapeutic innovation [15]. Furthermore, plant derived gums have shown potential in treating influenza [16], pulmonary tuberculosis and various gastrointestinal, urinary, and dermatological disorders, while exhibiting strong anti-inflammatory and detoxifying properties [17].

Here, we explored the therapeutic potential of gum obtained from *Prosopis juliflora* (PJ) plant, a widely prevalent and dominant plant species belonging to the leguminous family (Fabaceae). PJ is commonly found along roadsides as well as in arid, semi-arid regions, and degraded lands across the globe [18]. The gum derived from PJ (PJ-Gum) is a jelly-like, highly water-soluble exudate traditionally recognized for its numerous therapeutic and functional properties, including digestion and colon health management [19,20]. PJ-Gum has demonstrated significant potential for various industrial applications, particularly in the food, pharmaceutical and cosmetic sectors [21]. Moreover, previous studies have reported that PJ-Gum exhibits antimicrobial, anticancer and antidiabetic activities [22]. Being non-toxic and biodegradable and rich in secondary metabolites, complex polysaccharides and carboxyl functional groups. PJ-Gum serves as a natural reducing and capping agent in the green synthesis nanoparticles, thereby eliminating the need for toxic chemical reagents [23]. These multifunctional characteristics not only promote sustainable nanomaterial production but also enhance biological activity, making PJ-Gum a promising candidate for therapeutic and biomedical applications. Among diverse nanomaterials, bio-capped nanoparticles have gained increasing attention owing to their biocompatibility, biodegradability, superior biological activity and unique biochemical properties. Consequently, they have found a wide range of applications including drug delivery, wound healing, cancer therapy, antimicrobial activity, tissue engineering, diagnostics and therapeutic interventions. Among various metal-based nanoparticles, zinc oxide nanoparticles (ZnO NPs) have attracted particular interest due to their optical, catalytic, electrical, and antimicrobial properties [24,25]. The biosynthesis of ZnO NPs using plant-based materials, especially natural biopolymers such as plant gums, has emerged as a sustainable alternative to conventional synthesis methods, which often involve hazardous reagents, high energy consumption, and pose environmental risks [26]. Importantly, the U.S. Food and Drug Administration has recognized green-synthesized ZnO NPs as safe materials, thereby enhancing their translational potential in medical and pharmaceutical formulations.

In this study, we explored the therapeutic potential of bio-capped zinc oxide nanoparticles for a range of biomedical applications. PJ-Gum was employed as a sustainable capping agent for the synthesis of ZnO NPs, acting as both a reducing and stabilizing agent. This dual functionality facilitated nanoparticle formation while enhancing colloidal stability and biological activity [27,28]. Phytochemical profiling of PJ-Gum using LC-QTOF-MS confirmed the presence of numerous bioactive compounds with potential pharmacological relevance, which were further validated through in silico analysis. The phytochemicals present in PJ-Gum played a critical role in nanoparticle synthesis by mediating reduction and nucleation, as well as serving as capping and stabilizing agents. These molecules donate electrons to central metal ions, thereby facilitating the formation of capped and stable nanoparticle structures [29,30]. Additionally, PJ-Gum exhibits strong emulsifying and bioactive properties, enabling it to effectively reduce metal ions and maintain nanomaterial stability [31]. The synthesized nanoparticles were characterized using XRD, SEM, TEM, and XPS analyses, which confirmed the successful formation of PJ-Gum-capped ZnO NPs (G-ZnO). The biological activities of PJ-Gum and G-ZnO were evaluated through antimicrobial, antioxidant, anti-inflammatory, and antidiabetic assays. G-ZnO demonstrated superior therapeutic activity compared to pristine PJ-Gum, likely due to the effective decoration of bioactive compounds on the ZnO surface, which enhanced their biochemical reactivity. Overall, these findings highlight the potential of G-ZnO as a nature-derived, biocompatible, and multifunctional nanomaterial suitable for diverse biomedical applications, including wound healing, drug delivery, and tissue engineering.

2. Materials and methods

2.1. Extraction of Prosopis juliflora gum and synthesis of G-ZnO nanoparticles

Fresh gum was obtained from mature *Prosopis juliflora* trees located in Tirupati, Andhra Pradesh, India (13.6288° N, 79.4192° E). The collected material was immediately transported to the laboratory under sterile conditions. Taxonomic authentication of the plant material was carried out by cross-referencing with standard botanical databases and validated herbarium records. Surface contaminants were removed by forced air cleaning, after which the gum was air-dried at ambient temperature. The dried gum was finely ground using a sterile mechanical grinder and stored in airtight containers at room temperature until further use.

To synthesize ZnO nanoparticles via green chemistry, 20 mL of a 10% aqueous extract of PJ-Gum was prepared by filtering the gum solution through a 0.22 μm syringe filter (Sigma-Aldrich). The filtrate was heated at 70 °C with constant stirring for 30 min. Subsequently, 80 mL of 0.12 M zinc acetate dihydrate solution was added dropwise under continuous stirring at 70 °C. The pH of the mixture was adjusted to 10–12 by the gradual addition of 0.5 M NaOH to promote nanoparticle formation. The visible appearance of a white precipitate indicated the formation of ZnO. The reaction mixture was centrifuged at 8000 rpm for 10 min. The resulting pellet obtained was washed twice with distilled water (1:1, *v*/v) to remove unreacted precursors. The final product was oven-dried at 80 °C for 5 h. The dried ZnO NPs, hereafter referred to as Gum-ZnO NPs, (G-ZnO) were collected and preserved for further characterization and bioactivity assessments.

2.2. Characterization of PJ-gum and G-ZnO nanoparticles

To elucidate the functional groups involved in nanoparticle synthesis and stabilization, Fourier transform infrared (FT-IR) spectra of both the gum and G-ZnO NPs were recorded using a Jasco *V*-770 FT-IR spectrometer (Japan). Samples were scanned over the wavenumber range of 4000–500 cm^{-1} at a scan rate of 1 cm^{-1} per second. The optical properties of the synthesized nanoparticles were evaluated using a UV–Visible spectrophotometer (Varian Cary 100, Agilent Technologies, USA). Absorbance spectra were recorded in the 200–800 nm wavelength range, using distilled water as the reference blank. X-ray diffraction (XRD) analysis was conducted to determine the crystalline structure of the synthesized ZnO nanoparticles. Data were acquired using a Rigaku MPA-2000 diffractometer operated at 40 kV and 30 mA, scanning from 10° to 80° (2θ) with a step size of 0.02°. Powdered samples were mounted on a glass sample holder. The surface charge and colloidal

stability of Gum–ZnO NPs were determined by zeta potential measurements using a Zetasizer Nano ZS apparatus (Malvern Instruments, UK). Measurements were conducted in aqueous suspension at ambient temperature.

X-ray photoelectron spectroscopy (XPS) investigation was conducted using a Thermo Scientific K-Alpha™ XPS system with a monochromatic Al Kα X-ray source. Surveys and high-resolution scans were performed to determine the elemental composition and chemical states of the nanoparticles within a binding energy range of 100–4000 eV. The morphology and elemental distribution of PJ-Gum and G-ZnO NPs were examined using a HITACHI scanning electron microscope (SEM) operating at 5 keV. Samples were mounted on carbon-coated stubs and sputter-coated with gold to enhance conductivity. Elemental analysis was performed using energy dispersive X-ray (EDX) spectroscopy at an accelerating voltage of 20 keV. Transmission electron microscopy (TEM) was utilized to determine morphology, particle size, and dispersion of the synthesized nanoparticles. A drop of nanoparticle suspension was deposited onto a carbon-coated copper grid and subsequently dried under vacuum. Imaging was performed using a JEOL JEM-3010 TEM operating at 200 keV.

2.3. Preparation of Prosopis juliflora gum for metabolite identification

For metabolite identification, 10 mg of powdered gum was flash-frozen in liquid nitrogen and subsequently homogenized. The homogenate was transferred into 1.5 mL microcentrifuge tubes, followed by the addition of 1 mL methanol containing 0.1% formic acid subsequently added. Samples were vortexed for 10 min and incubated at −20 °C for 1 h to precipitate proteins and enhance metabolite solubilization. Post-incubation, samples were centrifuged at 10,000 rpm for a duration of 10 min. The resulting supernatant was collected and evaporated under vacuum conditions. The dried residue was diluted in 50 μL of methanol and subsequently analyzed using LC-MS with an Xevo G2-XS QToF mass spectrometer (Waters Corp., USA). Detailed LC gradient parameters, elution profiles, and mass spectrometry conditions are provided in Supplementary Tables S1–S3.

2.3.1. Metabolomic data analysis

An aliquot (5 μL) of the reconstituted extract was injected into an Ultra-Performance Liquid Chromatography coupled with Mass Spectrometry (UPLC-MS) system. Data acquisition was performed in positive electrospray ionization mode. Metabolite identification and spectral deconvolution were carried out using Progenesis QI software. The resulting data were further cross-validated against multiple chemical databases, including ChemSpider, KEGG, and PubChem, for comprehensive annotation of plant-derived secondary metabolites, following the workflow outlined by Blaženović et al. [32] and Tapfuma et al. [33].

2.4. Cell viability assay

A colorimetric MTT (3-(4,5-dimethylthiazol-2-yl)-2,5-diphenyltetrazolium bromide) assay was employed to assess cell viability based on metabolic activity. The experiment was conducted in a 96-well plate, with 1×10^4 HeLa cells seeded per well and incubated at 37 °C. Cells were treated with various concentrations of G-ZnO nanoparticles (1 mg/mL) for 24 h. The negative control group comprised cells exposed to medium alone. Following incubation, the supernatant was discarded, and the wells were rinsed twice with PBS. Subsequently, 10 μL of MTT solution was combined with 90 μL of medium (final volume 100 μL) and introduced into each well. The plates were wrapped in aluminum foil and incubated for 4 h to facilitate formazan crystal formation. Thereafter, 100 μL of DMSO was added to dissolve the crystals. Absorbance was measured at 517 nm, with a reference wavelength of 620 nm, using a BIO-RAD 680 microplate reader (USA). Each experiment was conducted in quintuplicate, and relative cell viability was determined as a percentage of the untreated control.

2.5. Preparation of bacterial and fungal cultures

Bacterial strains *Pseudomonas aeruginosa* (ATCC 9027), *Bacillus subtilis* (ATCC 6633), *Staphylococcus aureus* (ATCC 6538), and *Escherichia coli* (ATCC 8739), as well as fungal strains *Candida albicans* (ATCC 10231) and *Aspergillus niger* (ATCC 16404), were obtained from the Korean Culture Collection of Probiotics. Ampicillin (antibacterial control) and cycloheximide (antifungal control), along with all culture media, were purchased from Sigma-Aldrich, USA.

2.6. Antibacterial and antifungal activity

The antibacterial activity of the nanoparticles was evaluated using the agar well diffusion method against *P. aeruginosa*, *B. subtilis*, *S. aureus*, and *E. coli*. Ampicillin (100 μg/mL in sterile distilled water) served as the positive control. Nutrient agar medium was prepared by dissolving 7.4 g in 200 mL of distilled water, followed by autoclaving at 121 °C for 15 min. The medium was poured into sterile Petri dishes and solidified. Bacterial cultures were spread evenly using an L-shaped glass spreader. Wells were created, and nanoparticle samples at concentrations of 25, 50, 75, and 100 μg/mL were added. Inhibitory zones were measured with vernier calipers after 12 h of incubation at 37 °C.

Antifungal efficacy of synthesized nanoparticles was tested against *C. albicans* and *A. niger* using the well diffusion method. Cycloheximide (100 μg/mL in sterile distilled water) was used as the positive control. Potato dextrose agar (2.8 g in 75 mL distilled water) was autoclaved at 121 °C for 15 min, poured into Petri dishes, and solidified. Fungal cultures were spread evenly using an L-shaped glass rod. Nanoparticle concentrations (25, 50, 75, and 100 μg/mL) were introduced into wells, and plates were incubated at 28 °C for 48 h, after which inhibition zones were measured.

2.7. Live/dead cell staining assay

To evaluate the viability of *E. coli* (1×10^9 CFU mL^{-1}) cells treated with PJ-Gum and G-ZnO NPs, the LIVE/DEAD™ BacLight™ Bacterial Viability Kit (Invitrogen) was used. Cells were stained with SYTO 9 and propidium iodide according to the manufacturer's instructions and incubated in the dark for 60 min. Treated and control cells were visualized under a fluorescence microscope, and images were captured using Invitrogen live cell imaging software.

2.8. DPPH free radical scavenging activity

The antioxidant activity was evaluated using the 2,2-diphenyl-1-picrylhydrazyl (DPPH) assay following Almuhayawi et al. [34] with modifications. Briefly, 200 μL of DPPH solution (prepared in methanol) was added to each tube, followed by 200 μL of the sample at different concentrations (100–500 μg/mL). The mixtures were incubated in the absence of light at room temperature for 30 min. Absorbance was measured at 517 nm using a spectrophotometer, with ascorbic acid as the reference standard. Both gum and gum-capped ZnO NPs were tested. DPPH scavenging activity (%) was calculated using the formula:

$$\%\text{DPPH scavenging activity} = \left[\left(\text{Abs}_{\text{control}} - \text{Abs}_{\text{sample}}\right)/\text{Abs}_{\text{control}}\right] \text{X } 100$$

2.9. Molecular docking

Primary virtual screening of 12 components identified from gum via LC-QTOF analysis was conducted against four antimicrobial proteins using PyRx and CB-Dock2. The top-ranked compound, based on binding affinity, was further docked using Maestro 13.0 (Schrödinger). Ligands and protein structures were prepared using LigPrep and the Protein Preparation Wizard. Water molecules were removed, bond orders assigned, hydrogen atoms added, and protonation states optimized. The

H-bond network was refined, and torsion parameters were adjusted with an RMSD of 0.30 Å. Ligands from PubChem were converted into 3D optimized forms considering tautomeric, stereochemical, and ionization states. Docking was performed using Glide in standard precision mode with extensive sampling. Receptor grids (10 Å × 10 Å × 10 Å) were generated with a Van der Waals scaling factor of 1.0 and partial charge cut-off of 0.25. Target proteins (PDB IDs: 1JIJ, 1JX9, 3SRW, and 1AJ6) were used for active site docking.

2.10. Antidiabetic and anti-inflammatory activity

The antidiabetic potential of PJ-Gum and G-ZnO was assessed by measuring the inhibition of α-amylase activity using fluorescence spectroscopy, as described by Avwioroko et al. [35] with modifications. Freshly prepared α-amylase (0.5 mg/mL in PBS, pH 7.1) was incubated with PJ-Gum and G-ZnO at concentrations of 100–600 μg/mL for 30 min in the dark. Fluorescence spectra were acquired using an excitation wavelength of 280 nm, and emission spectra were recorded within the range of 300–500 nm. The degree of fluorescence quenching was used to infer enzyme inhibition.

2.11. Statistical analysis

All experiments were performed in triplicate ($n = 3$), and data are presented as mean ± standard error (SE). For each assay-antimicrobial zone of inhibition, cell viability, and anti-inflammatory activity-differences among treatments (PJ-Gum, G-ZnO nanoparticles, and the positive control) were analyzed using one-way ANOVA, followed by Dunnett's post-hoc test to compare each treatment with the control. Statistical analyses were conducted in GraphPad Prism (version 10), with summary calculations/plotting assisted by Microsoft Excel 2019. Differences were considered statistically significant if the two-tailed p-value was less than 0.05.

3. Results and discussion

3.1. LC-QTOF –MS analysis of PJ-gum

The phytochemical composition of *Prosopis juliflora* gum (PJ-Gum) was analyzed using LC–QTOF–MS. This study presents the first comprehensive metabolomic profiling of PJ-Gum aimed at elucidating its chemical diversity and potential biological functionality. The chromatographic analysis revealed a broad spectrum of low molecular weight phytochemicals, tentatively identified based on their exact masses, retention times, and MS/MS fragmentation patterns (Fig. S1). Database-assisted annotation combined with literature comparison facilitated the identification of several bioactive metabolites with established antimicrobial and antioxidant activities. Representative chemical structures of the predominant compounds are illustrated in Fig. 1, and their analytical characteristics are summarized in Table 1.

The identified metabolites were categorized into major structural classes, including flavonoids, phenolic acids, terpenoids, sterols, and alkaloids, each known to contribute to the overall biological functionality of the gum. In total, 145 distinct compounds were detected and annotated (Table S4), highlighting the remarkable phytochemical complexity of PJ-Gum. This chemical diversity reflects its multifunctional nature, enabling it to serve both as a reducing and stabilizing agent in nanoparticle synthesis. Specifically, the redox-active phenolics and flavonoids facilitate the nucleation and reduction of Zn^{2+} ions during ZnO nanoparticle formation, while the amphiphilic polysaccharide–terpenoid matrix imparts steric stabilization and biocompatible surface coating. Therefore, LC–QTOF–MS profiling not only delineates the molecular identity of PJ-Gum but also provides mechanistic insight into how its intrinsic phytochemical constituents govern the formation, stability, and enhanced biological performance of G-ZnO nanoparticles described in subsequent sections.

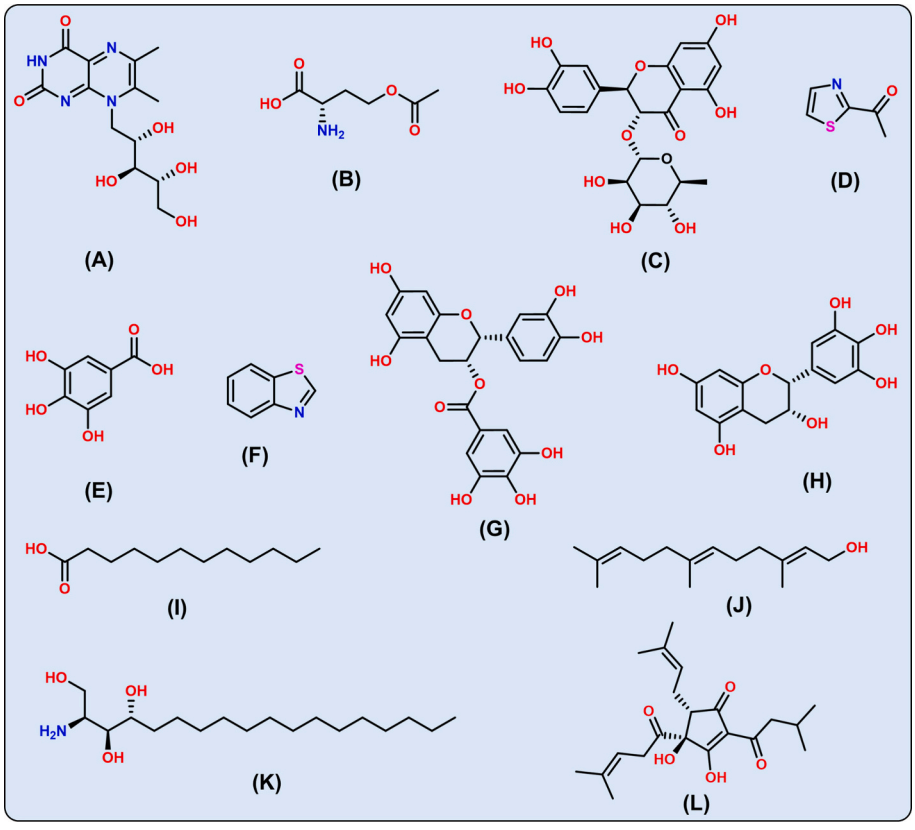

Fig. 1. Chemical structures of major antimicrobial compounds identified in *Prosopis juliflora* gum.

Table 1
Antimicrobial compounds identified in *Prosopis juliflora* gum using UHPLC- ES-QTOF-MS with supporting reference.

S. No.	RT (min)	Proposed compound	Measured *m/z*	Formula	Chemical structure	Cosine score	Ref.
1	1.251	6,7- Dimethyl-8-(1-D-Ribityl) Lumazine	365.0783	$C_{13}H_{18}N_4O_6$	(A)	50.1	[36]
2	1.251	O-Acetyl-L-homoserine	184.0559	$C_6H_{11}NO_4$	(B)	27	[37]
3	1.261	Astilbin	489.0798	$C_{21}H_{22}O_{11}$	(C)	48.4	[38]
4	1.602	2-Acetylthiazole	128.0187	C_5H_5NOS	(D)	24.1	[39]
5	1.881	Gallic acid	171.0294	$C_7H_6O_5$	(E)	37.5	[40]
6	2.842	Benzothiazole	158.0015	C_7H_5NS	(F)	34.5	[41]
7	13.375	Epicatechin gallate	443.0965	$C_{22}H_{18}O_{10}$	(G)	51.4	[42]
8	16.630	Epigallocatechin	329.068	$C_{15}H_{14}O_7$	(H)	33.5	[42]
9	17.509	Lauric acid	218.2099	$C_{12}H_{24}O_2$	(I)	36.9	[43]
10	30.688	2-trans,6-trans-Farnesol	240.2314	$C_{15}H_{26}O$	(J)	37.6	[44]
11	30.801	Phytosphingosine	318.2993	$C_{18}H_{39}NO_3$	(K)	57.7	[45]
12	43.900	Trans-Isohumulone	363.2178	$C_{21}H_{30}O_5$	(L)	39.8	[46]

3.2. Optical properties of gum and G-ZnO nanoparticles

The UV–Visible absorption spectrum of native PJ-Gum exhibited a distinct peak at 278 nm, corresponding to π → π* electronic transitions of aromatic rings and n → π* transitions of carbonyl groups present in phenolic and flavonoid constituents (Fig. 2A). Following nanoparticle synthesis, a pronounced red shift was observed, with a new absorption maximum appearing at 367 nm. This band is characteristic of the surface plasmon resonance (SPR) of ZnO nanoparticles, confirming the successful formation of nanostructures. The observed bathochromic shift indicates a strong interaction between ZnO and the phytochemical moieties of PJ-Gum, suggesting active participation of biomolecules in both surface reduction and capping processes. Similar red shifts have been reported in other biopolymer-mediated ZnO nanoparticle systems, where the conjugation of organic molecules modulates the local electronic environment of ZnO. To further elucidate the chemical

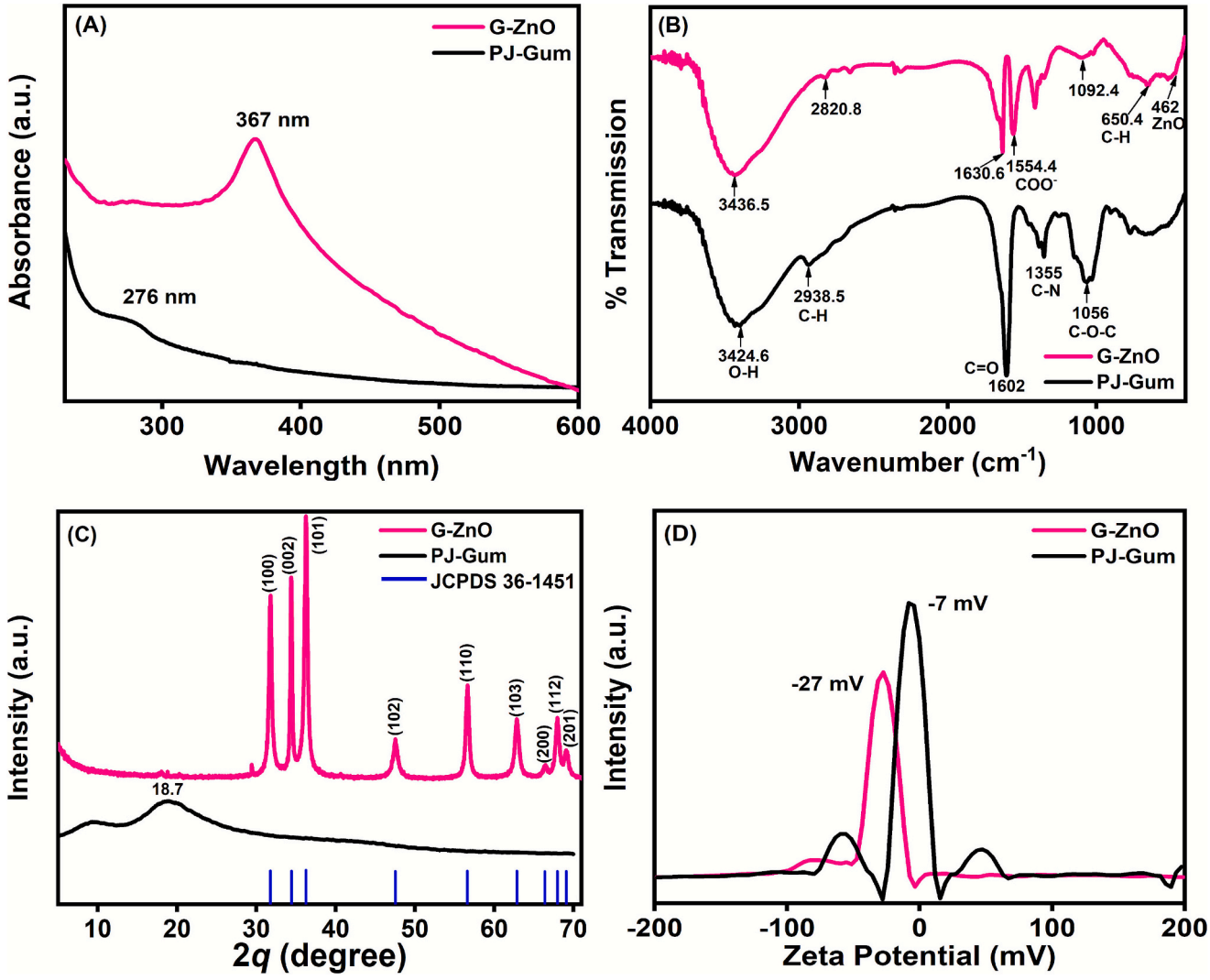

Fig. 2. (A) UV–Vis spectra of PJ-Gum and G-ZnO nanoparticles; (B) FT-IR spectra of PJ-Gum and G-ZnO; (C) XRD patterns of PJ-Gum and G-ZnO; (D) Zeta potential measurements of PJ-Gum and G-ZnO.

interactions responsible for nanoparticle stabilization, FT–IR spectra of both PJ-Gum and G-ZnO were analyzed (Fig. 2B). The FT–IR spectrum of native PJ-Gum displayed a broad O—H stretching band at 3424.6 cm^{-1}, indicative of abundant hydroxyl groups originating from polysaccharides and phenolic compounds. A characteristic C—H stretching vibration appeared at 2938.5 cm^{-1}, representing aliphatic hydrocarbon groups. Additional peaks at 1602 cm^{-1} and 1355 cm^{-1} corresponded to asymmetric carboxylate (COO^{-}) and C–O–C (aromatic ether) stretching vibrations, respectively, highlighting the complex polyhydroxylated and carbohydrate-rich nature of PJ-Gum. In the case of G-ZnO, new absorption bands appeared at 462 and 650.4 cm^{-1}, where the band at 462 cm^{-1}, corresponding to Zn—O stretching vibrations, confirming the successful incorporation of ZnO into the matrix, while the band at 650.4 cm^{-1} was attributed to C—H bending vibration of alkyne-related groups derived from the gum extract. These changes suggest coordination of the gum carboxyl and amide groups with Zn^{2+}, confirming the preservation of bioactive moieties after synthesis. C—H stretching vibrations of alkanes were also detected at 2820.8 cm^{-1}, further confirming retention of bioactive moieties from the gum matrix. These spectral features collectively demonstrate the coexistence of gum functional groups with ZnO. This not only confirms successful capping and stabilization but also indicates the presence of functional groups on the nanoparticle surface, thereby enhancing stability and bioactivity [47].

3.3. Crystalline structure, surface charge, and size distribution of G-ZnO nanoparticles

The crystalline phase composition of PJ-Gum and PJ-Gum–ZnO nanoparticles (G-ZnO NPs) was analyzed using X-ray diffraction (XRD) patterns (Fig. 2C). The diffraction profile of native PJ-Gum exhibited no sharp reflection peaks, showing broad humps at 2θ values of 9.3° and 18.7°, indicative of an amorphous, non-crystalline biopolymer matrix. In contrast, the G-ZnO NPs displayed several sharp and intense diffraction peaks corresponding to the (100), (002), (101), (102), (110), (103), (200), (112), and (201) planes, with respective 2θ values of 31.76°, 34.46°, 36.24°, 47.48°, 56.70°, 62.91°, 66.34°, 68.03°, and 69.27°. These peaks confirm the highly crystalline and single-phase nature of the synthesized nanoparticles, consistent with the hexagonal wurtzite structure of ZnO and matching the standard JCPDS card number 36–1451 [48]. The absence of extraneous peaks further verifies the phase purity of the nanoparticles and demonstrates that the gum matrix effectively facilitated the nucleation and growth of ZnO crystallites while preventing secondary phase formation.

To assess the surface charge and colloidal stability of the synthesized nanoparticles, zeta potential (ZP) measurements were performed (Fig. 2D). The native PJ-Gum exhibited a ZP of −7 mV, indicating weak electrostatic repulsion typical of biopolymer solutions. In contrast, the G-ZnO nanoparticles showed a markedly higher negative potential of −27 mV, signifying enhanced surface charge density following nanoparticle formation. This shift can be attributed to the adsorption of hydroxylated Zn species and deprotonated functional groups (e.g., $–COO^{-}$, –OH) derived from the gum matrix. The pronounced negative surface charge suggests strong electrostatic repulsion among particles, which minimizes aggregation and contributes to excellent colloidal stability. Additionally, Van der Waals and steric interactions imparted by the polysaccharide–terpenoid components of PJ-Gum likely aid in maintaining nanoparticle dispersion and stability in suspension [49]. During synthesis, negatively charged organic moieties from the gum matrix interact with positively charged Zn^{2+} ions, forming a capping layer that restricts uncontrolled growth and aggregation. This capping effect reduces surface and interfacial tension, thereby lowering cohesive forces at the interface and imparting favorable emulsifying characteristics to the nanostructure [50,51].

3.4. X-ray photoelectron spectroscopy analysis of PJ-gum and G-ZnO NPs

XPS was employed to determine the elemental composition and chemical states of pristine PJ-Gum and the synthesized G-ZnO. The wide-scan XPS survey spectrum of the native PJ-Gum revealed the presence of C 1s, O 1s, and Si 2p peaks located at binding energies of 258.03 eV, 532.14 eV, and 101.09 eV, respectively (Fig. 3A). High-resolution deconvolution of the C 1s spectrum identified four distinct peaks at 282.89, 284.60, 286.58, and 288.32 eV, which were assigned to C—Si, C–C/C=C, C—O, and C═O bonding environments, respectively (Fig. 3B). The O 1s spectrum was resolved into five components at 528.07, 529.66, 530.93, 532.40, and 533.50 eV, corresponding to Si—O, C—O, C–O–C, C–OH, and O–C=O groups, respectively (Fig. 3C). A distinct peak observed at 101.4 eV in the high-resolution Si 2p spectrum confirmed the presence of silicon in the form of organosilicon moieties (Fig. 3D). These findings suggest that the native PJ-Gum matrix is primarily composed of carbohydrate and phenolic structures interlinked with trace organosilicon constituents, which may influence its surface reactivity and ability to chelate metal ions.

Upon capping ZnO nanoparticles with the gum, the XPS spectrum of G-ZnO NPs revealed the appearance of additional elemental peaks corresponding to Zn 2p and Na 1s, alongside C 1s and O 1s (Fig. 4A). These were recorded at binding energies of 258.02 eV (C 1s), 531.14 eV (O 1s), 1021.07 eV (Zn 2p), and 1070.81 eV (Na 1s). The high-resolution C 1s spectrum exhibited three peaks at 285.08, 286.94, and 288.52 eV, assigned to C–C/C=C, C—O, and C═O functionalities, respectively (Fig. 4B). The O 1s spectrum was deconvoluted into four peaks at 529.76, 530.86, 531.57, and 535.40 eV, attributed to Zn–O/C–O, Zn–OH/C–OH, C═O, and O–C=O species, respectively (Fig. 4C). The Zn 2p spectrum displayed two prominent spin-orbit doublets at 1020.6 eV and 1043.71 eV, corresponding to Zn $2p_{3/2}$ and Zn $2p_{1/2}$, respectively. Additional signals at 1018.23 eV and 1040.71 eV were attributed to metallic ZnO, confirming the presence of Zn in both oxidized and reduced forms (Fig. 4D). The Na 1s spectrum exhibited three deconvoluted peaks at 1068.72, 1070.33, and 1071.96 eV, corresponding to elemental Na^{0}, lattice-bound Na^{+}, and Na_2O, respectively (Fig. 4E).

The obtained XPS data confirm the successful integration of ZnO nanoparticles within the PJ-Gum matrix and the coexistence of organic and inorganic chemical states. The identified Zn^{2+}, Zn—O, and Zn–OH components validate the formation of ZnO nanoparticles, while the persistence of C—O, C═O, and O–C=O functionalities indicates the retention of gum-derived biomolecules on the nanoparticle surface. These observations are consistent with FT–IR findings and provide strong evidence for chemical interactions between the bioactive functional groups of PJ-Gum and Zn^{2+} ions during synthesis. The results further substantiate the dual role of PJ-Gum as a natural reducing and stabilizing agent in the green synthesis of ZnO nanoparticles.

3.5. Morphological and elemental characterization of PJ-gum and G-ZnO NPs

SEM micrographs of pristine PJ-Gum at different magnifications (Fig. 5A and B) revealed irregular, non-crystalline structures of varying sizes with a rough surface texture and visible surface cracks, which are typical features of natural plant-derived biopolymers. These morphological characteristics confirm the amorphous and heterogeneous nature of the gum matrix. Elemental mapping using Energy-Dispersive X-ray (EDX) analysis (Fig. S14) confirmed the predominant presence of carbon (C), oxygen (O), and nitrogen (N), consistent with the polysaccharide and proteinaceous composition of the gum.

In contrast, the SEM images of G-ZnO nanoparticles (Fig. 5C and D) demonstrated a more organized morphology with distinct spherical nanoparticle formations embedded within and around the gum matrix. The nanoparticles appeared uniformly distributed with a wrinkled surface morphology, suggesting effective capping and stabilization by the gum. The spherical geometry and nanoscale texture of the particles were

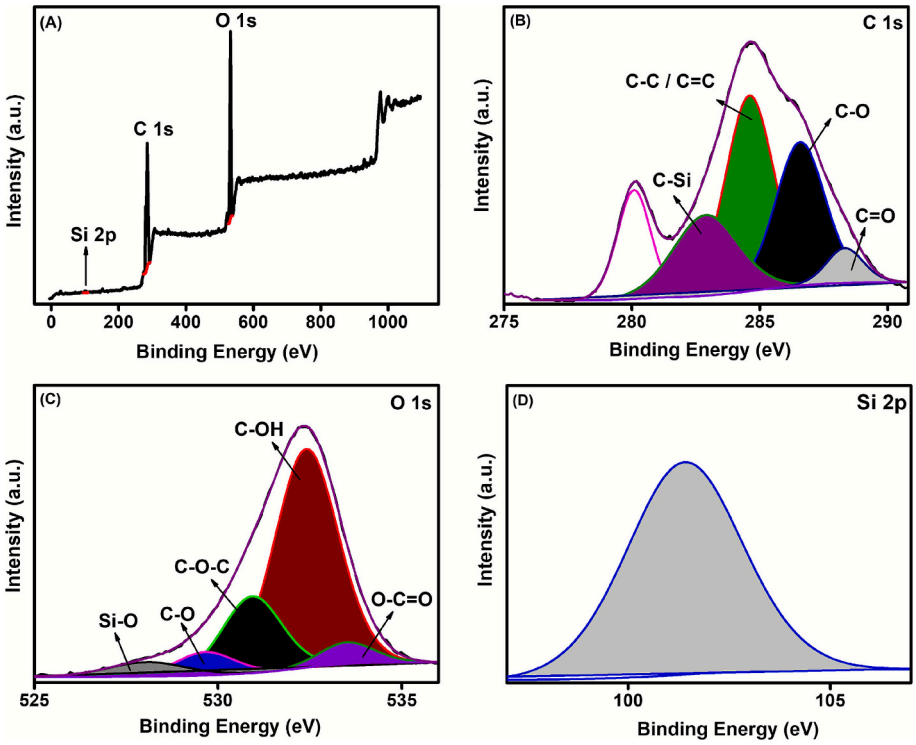

Fig. 3. XPS of *Prosopis juliflora* gum: (A) Total survey spectrum; (B—D) High-resolution spectra for C 1s, O 1s, and Si 2p, respectively.

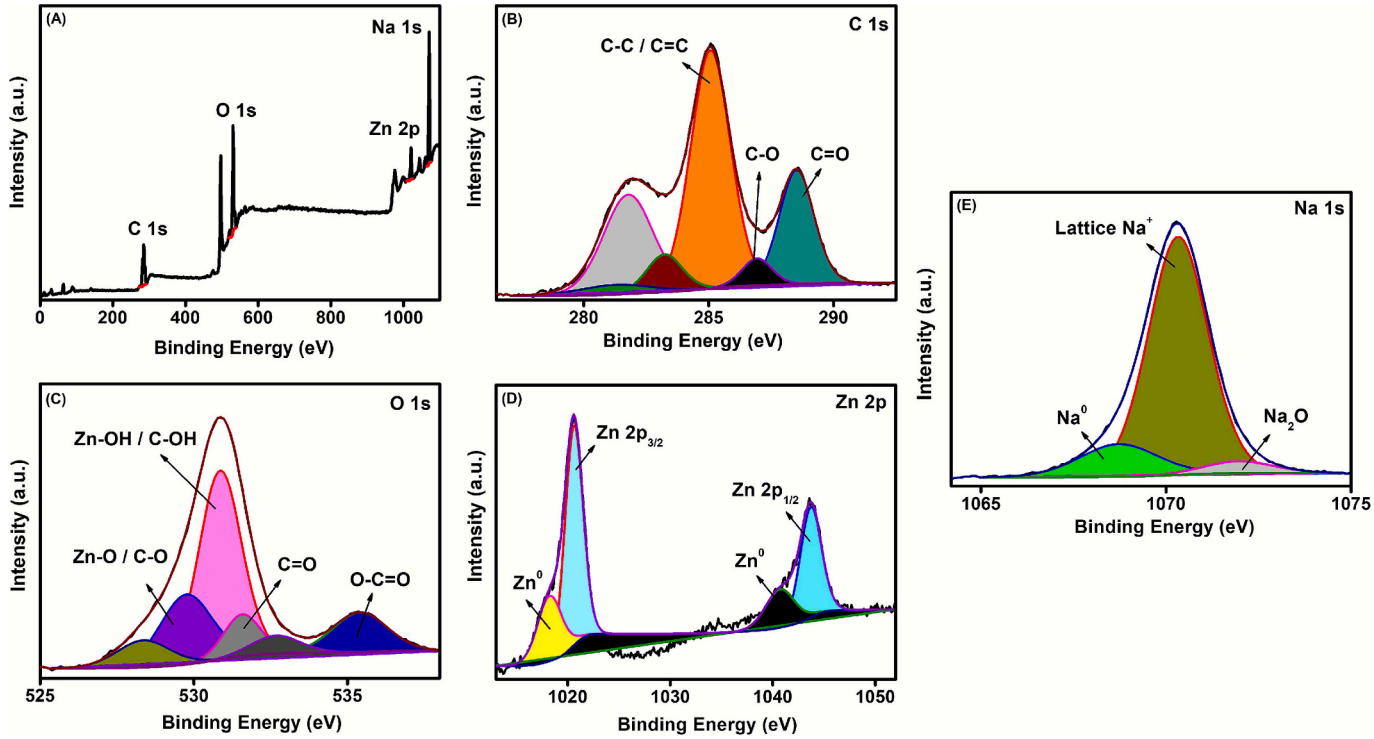

Fig. 4. XPS analysis of G-ZnO nanoparticles: (A) Total survey spectrum; (B–E) High-resolution spectra of C 1s, O 1s, Zn 2p, and Na 1s.

clearly visualized, indicating successful ZnO nucleation on the bio-polymeric environment. Elemental mapping of G-ZnO revealed uniform distribution of the major elements C, N, O, and Zn, further validated by the EDX spectrum (Fig. 5E and F). The detection of Zn strongly confirms the successful formation and incorporation of zinc oxide within the PJ-Gum scaffold.

TEM provided further insights into the internal morphology and size distribution of both PJ-Gum and G-ZnO (Fig. 6). The TEM image of gum (Fig. 6A) showed irregular, thin-layered, and overlapping amorphous structures, characteristic of natural plant-derived polysaccharide-based materials. In contrast, the TEM image of G-ZnO NPs (Fig. 6B) revealed uniformly distributed, well-defined spherical nanoparticles. The

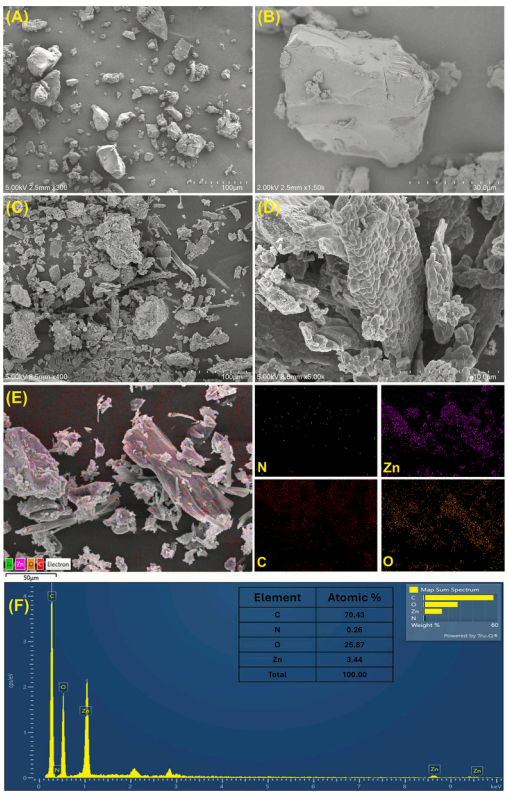

Fig. 5. (A & B) SEM images of PJ-Gum; (C & D) SEM images of G-ZnO at different magnifications; (E) EDX spectrum showing elemental composition of G-ZnO; (F) Elemental mapping of G-ZnO.

magnified view (Fig. 6C) displayed fragmented and porous granular nano-dot structures with an average particle size of approximately 34.1 nm. The well-resolved lattice fringes observed in high-resolution TEM images confirmed the crystalline nature of the nanoparticles, in agreement with XRD and XPS results. On the other hand, the hydrodynamic behavior of G-ZnO NPs in aqueous suspension was evaluated using Dynamic Light Scattering (DLS) analysis, which revealed an average particle size of 147.1 nm with a polydispersity index (PDI) of 0.406 (Fig. 6D), indicating moderate monodispersity. The relatively larger hydrodynamic size compared to the TEM-derived particle size is an expected outcome, as DLS measurements reflect the solvated and dispersed state of nanoparticles, accounting for the hydration layer, gum-mediated capping, and interparticle interactions in the colloidal system, whereas TEM depicts the dry-state core dimensions under vacuum conditions. Although some degree of aggregation was observed, the overall particle population remained predominantly nanoscale and well-dispersed [52]. These complementary SEM, EDX, TEM, and DLS findings confirm the efficient bio-reduction, capping, and stabilization of ZnO nanoparticles by *Prosopis juliflora* gum. The gum's inherent biopolymeric nature and rich phytochemical profile not only facilitated nanoparticle formation but also contributed to enhanced structural uniformity, stability, and surface functionality, attributes that are expected to improve their physicochemical and biological performance in subsequent applications.

3.6. Antioxidant activity: DPPH radical scavenging assay

The antioxidant potential of PJ-Gum and G-ZnO nanoparticles was assessed through the 2,2-diphenyl-1-picrylhydrazyl (DPPH) radical scavenging assay. Ascorbic acid served as the reference standard. The assay measures the ability of the test compounds to donate hydrogen atoms or electrons to neutralize DPPH free radicals, resulting in a decrease in absorbance at 517 nm. The extent of DPPH radical inhibition was quantified spectrophotometrically. Fig. 7A illustrates the antioxidant activity of standard ascorbic acid, which showed a strong linear dose-response relationship with a coefficient of determination (R^2) value of 0.9967, indicating excellent free radical scavenging capacity. Similarly, the gum extract displayed robust antioxidant activity, with an R^2 value of 0.9832 (Fig. 7B). This activity is attributed to the high content of polyphenolic and flavonoid constituents in the gum, which possess strong redox potential and are capable of donating electrons or hydrogen atoms to stabilize reactive free radicals [53].

Remarkably, the gum-capped ZnO nanoparticles (G-ZnO NPs) exhibited even greater antioxidant activity compared to the native gum (Fig. 7C), with an R^2 value of 0.9986. This enhancement suggests a synergistic interaction between the phytoconstituents of PJ-Gum and the ZnO nanostructures. The coupling of phenolic and flavonoid biomolecules with ZnO surfaces is known to increase electron density and promote redox cycling, thereby amplifying the overall radical scavenging capacity [54]. Such surface functionalization likely improves charge transfer efficiency and stabilizes intermediate radicals formed during DPPH reduction. Fig. 7D presents the comparative regression curves of the different treatments, highlighting the superior performance of G-ZnO. A schematic representation of the proposed antioxidant mechanism is provided in Fig. 7E, illustrating how the bioactive phytochemicals of PJ-Gum interact with the ZnO nanoparticle surface to enhance electron transfer and reactive oxygen species (ROS) neutralization. These observations suggest that the hybrid nanocomposite combines the intrinsic redox activity of ZnO with the biological reducing power of gum-derived metabolites. These findings confirm that G-ZnO nanoparticles possess remarkable antioxidant potential, surpassing that of the parent gum. The enhanced radical scavenging efficiency arises from the synergistic effects between the metal oxide core and the organic capping matrix, underscoring the multifunctional applicability of G-ZnO in biomedical, nutraceutical, and antioxidant-based therapeutic formulations.

3.7. Antimicrobial activity of PJ-gum and G-ZnO nanoparticles

The antimicrobial potential of PJ-Gum and G-ZnO NPs was investigated against six clinically relevant pathogens; four bacterial strains (*Bacillus subtilis*, *Staphylococcus aureus*, *Escherichia coli*, and *Pseudomonas aeruginosa*) and two fungal species (*Aspergillus niger* and *Candida albicans*). The agar well diffusion assay was performed at a standardized concentration of 10 mg/mL, and inhibition zones were measured post-incubation using vernier calipers (Fig. 8A–F). The strongest zone of inhibition was recorded against *B. subtilis* and *P. aeruginosa*, with mean ± SD values of 7.2 ± 0.31 mm (PJ-Gum, *B. subtilis*), 7.0 ± 0.2 mm (PJ-Gum, *P. aeruginosa*), 8.8 ± 0.2 mm (G-ZnO, *B. subtilis*), and 8.9 ± 0.12 mm (G-ZnO, *P. aeruginosa*), compared to 9.5 ± 0.64 mm and 9.1 ± 1.1 mm for the ampicillin controls, respectively. At 100 μg/mL, G-ZnO exhibited statistically greater inhibition than PJ-Gum ($p < 0.01$), confirming enhanced antimicrobial efficacy (full ANOVA outputs in Supplementary Table S5).

Similarly, antifungal activity was significantly enhanced following nanoparticle synthesis. *A. niger* and *C. albicans* displayed inhibition zones of 2.2 ± 0.64 mm and 1.86 ± 0.11 cm for G-ZnO, respectively, compared to 0.2 ± 0.01 mm and 0.1 ± 0.02 mm for PJ-Gum, while standard antifungal agents yielded 1.8 ± 0.52 mm and 1.1 ± 0.25 mm, respectively. Although the antifungal activity of G-ZnO was comparatively lower than standard drugs, the enhancement over the native gum confirms the contribution of the nanoparticle component to fungal inhibition. Statistical analysis performed using one-way ANOVA followed by pairwise comparisons with positive controls (ampicillin for bacteria, cycloheximide for fungi) indicated significant differences ($p < 0.05$) between PJ-Gum and G-ZnO treatments for most strains.

The superior antimicrobial performance of G-ZnO can be ascribed to the synergistic interplay between the ZnO core and the gum phytoconstituents. The nanoparticles' small size and high surface-to-volume ratio

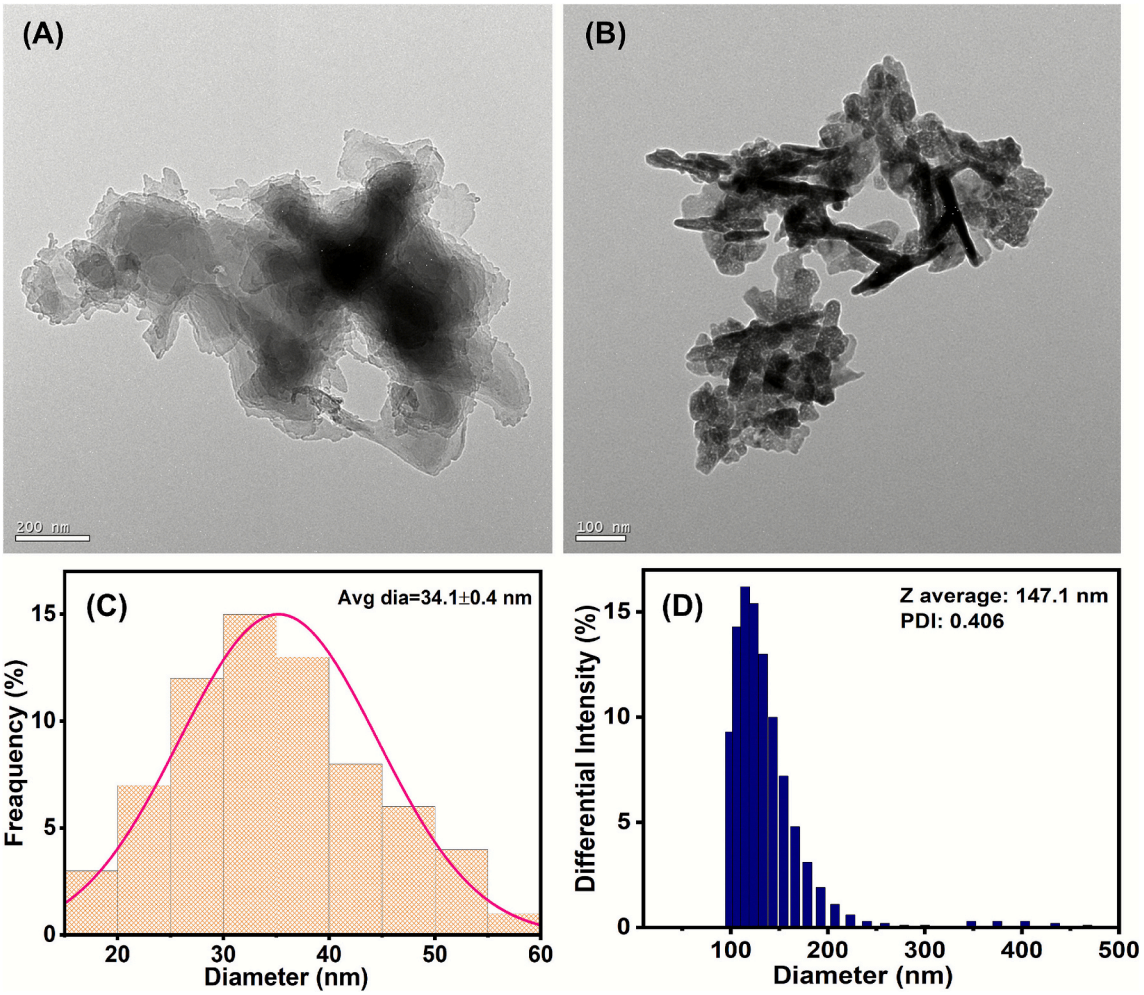

Fig. 6. High-resolution transmission electron microscopy (HR-TEM) images of: (A) PJ-Gum and (B) G-ZnO NPs; (C) Particle size distribution plot from TEM analysis; (D) Particle size distribution plot from DLS measurements.

promote strong adhesion to microbial membranes, leading to structural disruption, leakage of intracellular contents, and cell death via ROS generation and Zn^{2+} ion release [55,56]. Additionally, the phenolic, flavonoid, and terpenoid compounds present in the gum act as natural capping agents, stabilizing the nanoparticles and contributing intrinsic antimicrobial properties. The antifungal activity of G-ZnO was also noteworthy (Fig. 8E–F). Despite the greater complexity of fungal cell walls and membranes due to their eukaryotic composition, G-ZnO effectively inhibited fungal growth, likely due to strong nanoparticle–membrane interactions and the oxidative stress generated at the interface. The gum-derived biopolymeric capping layer further enhances antifungal action by interfering with fungal enzymatic activity, membrane receptor binding, and signal transduction pathways, as well as by preventing biofilm formation, particularly in *S. aureus* [57]. G-ZnO demonstrated broad-spectrum antimicrobial and antifungal activities comparable to standard antibiotics, underscoring their potential as a biocompatible, multifunctional antimicrobial agent. The synergistic redox and surface chemistry between ZnO nanostructures and the bioactive gum matrix render this nanocomposite a promising candidate for biomedical coatings, wound healing dressings, and infection-control materials.

3.8. Live/dead bacterial viability assay

A live/dead bacterial viability assay was performed to visualize the bactericidal efficacy of *E. coli* cells exposed to PJ-Gum and G-ZnO. Fluorescent staining differentiated viable (green fluorescence) from non-viable (red fluorescence) cells, as depicted in Fig. 9. The untreated control (Fig. 9A) exhibited predominantly green fluorescence, indicating metabolically active and intact *E. coli* cells. In contrast, bacterial cultures treated with PJ-Gum and G-ZnO, an increase in red fluorescence was noted in a dose-dependent manner, signifying enhanced bacterial membrane disruption and cell death (Fig. 9B–E). Remarkably, the G-ZnO induced substantially higher red fluorescence compared to PJ-Gum at equivalent concentrations, reflecting enhanced bactericidal potency of the nanocomposite. This finding corroborates the results of the agar well diffusion assay, confirming that nanoparticle incorporation significantly amplifies antibacterial efficacy, even at relatively low doses. The underlying antimicrobial mechanism is attributed to the synergistic action between ZnO nanoparticles and the phytochemical constituents of PJ-Gum. The ZnO core facilitates the generation of ROS, including hydroxyl radicals ($^{\bullet}OH$) and superoxide anions ($O_2^{-\bullet}$), which induce oxidative stress and lipid peroxidation in bacterial membranes. Concurrently, the bioactive flavonoids, phenolics, and terpenoids in the gum matrix enhance membrane permeability and interfere with essential cellular processes. These combined effects result in irreversible membrane disruption, leakage of cytoplasmic contents, and eventual bacterial death.

3.9. Cytocompatibility evaluation using MTT assay

The cytocompatibility of PJ-Gum and G-ZnO was evaluated using the

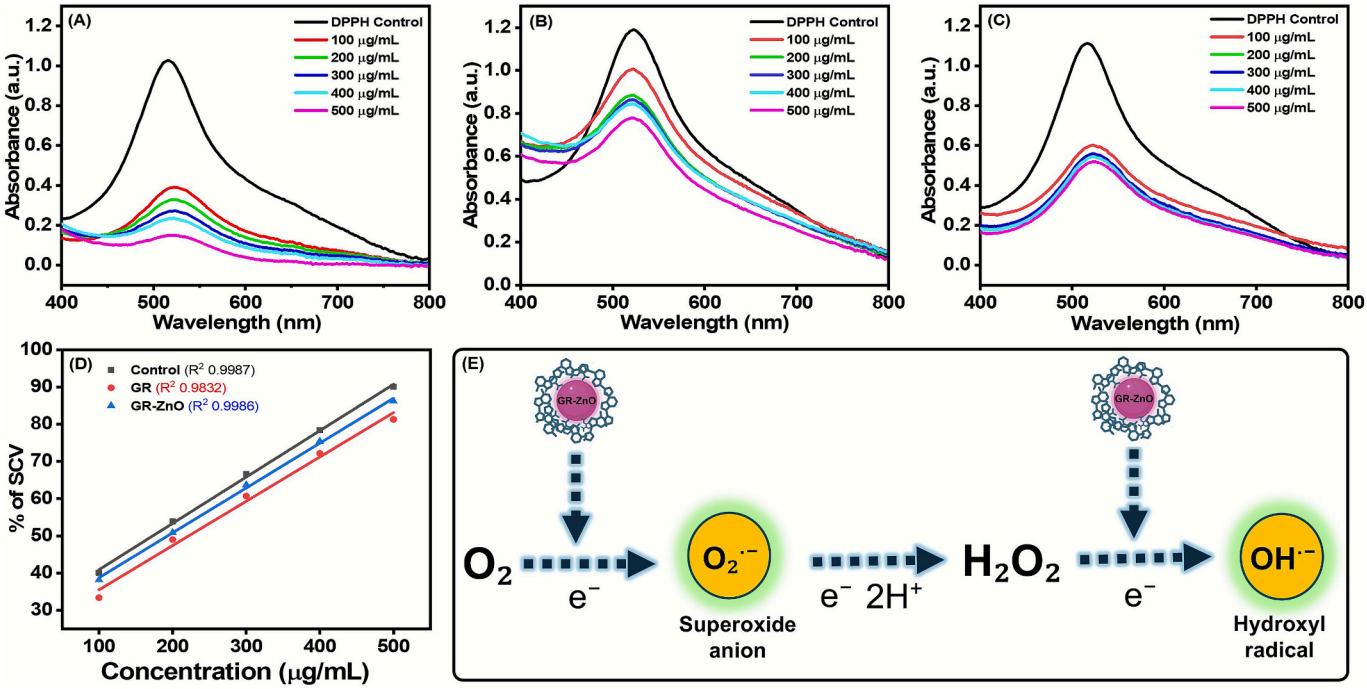

Fig. 7. Antioxidant activity of samples evaluated by DPPH (2,2-diphenyl-1-picrylhydrazyl) assay:(A) Standard ascorbic acid; (B) PJ-Gum, (C) G-ZnO across concentrations (100–500 μg/mL), (D) Comparative standard curve with R^2 values; (E) schematic representation of the proposed mechanism of antioxidant action for G-ZnO.

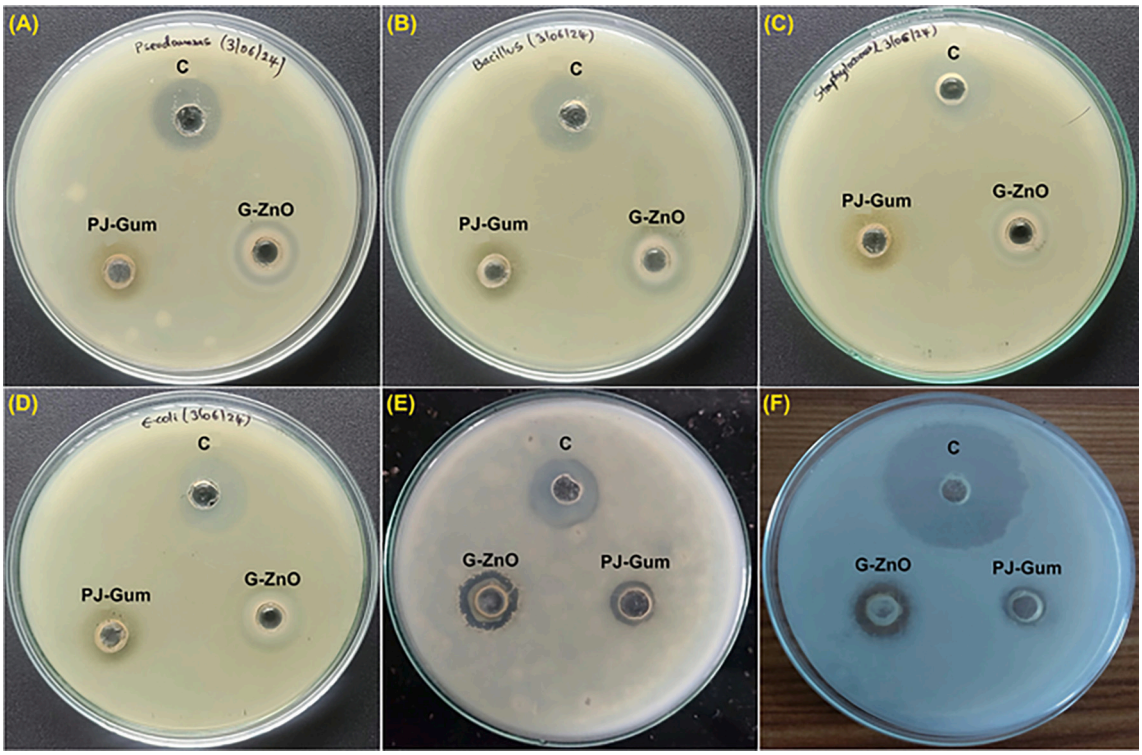

Fig. 8. Antibacterial and antifungal activities of PJ-Gum and G-ZnO NPs. (A) *Pseudomonas aureginosa,* (B) *Bacillus subtilis.* (C) *Staphylococcus aureus.* (D) *Escherichia Coli.* (E) *Aspergillus niger* and (F) *Candida albicans.* The inhibition zone diameters were measured after incubation, demonstrating the enhanced antimicrobial efficacy of the nanoparticle formulation compared to the native gum.

MTT [3-(4,5-dimethylthiazol-2-yl)-2,5-diphenyl tetrazolium bromide] assay to determine their effects on cellular metabolic activity in HeLa cells. Cells were seeded at a density of 1×10^4 cells per well in 96-well plates and treated with varying concentrations (0, 10, 25, 50, 75, and 100 μg/mL) of PJ-Gum and G-ZnO NPs for 24 h at 37 °C under standard culture conditions. Following incubation, MTT reagent was added to each well, and the resulting formazan crystals were solubilized and quantified spectrophotometrically at 490 nm using a microplate reader.

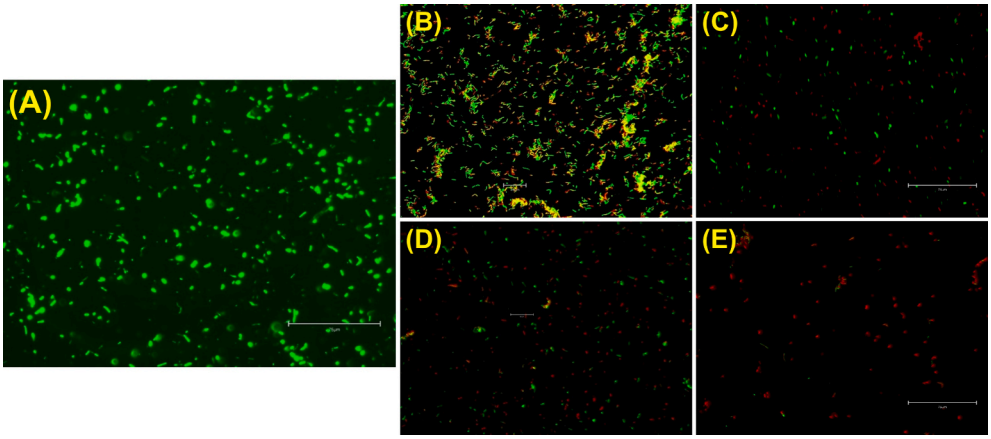

Fig. 9. Live/dead staining assay of *E. coli*: (A) Untreated control; (B) PJ-Gum at 25 mg/mL; (C) PJ-Gum at 50 mg/mL; (D) G-ZnO at 25 mg/mL; (E) G-ZnO at 50 mg/mL. Green fluorescence indicates viable cells, while red fluorescence represents membrane-compromised or dead cells.

The percentage of viable cells was calculated relative to untreated controls. As illustrated in Fig. 10, both PJ-Gum and G-ZnO maintained high levels of cell viability across all tested concentrations, demonstrating good biocompatibility. At 50 μg/mL, cell viability remained at 94.2% for PJ-Gum and 91.1% for G-ZnO. Even at the highest tested concentration (100 μg/mL), both materials exhibited cell viabilities above the cytotoxicity threshold, with 91.2% for PJ-Gum and 85.5% for G-ZnO. Although a slight decrease in viability was observed for G-ZnO relative to PJ-Gum, the reduction was not statistically significant ($p > 0.05$).

According to the ISO 10993-5 guidelines for biological evaluation of medical devices, materials maintaining ≥80% cell viability are considered non [58,59]. Based on this standard, both PJ-Gum and G-ZnO demonstrated excellent cytocompatibility, indicating that the biomaterial and its nanocomposite formulation are safe for potential biomedical applications. The slight reduction in viability observed for G-ZnO at higher concentrations can be attributed to mild oxidative stress arising from limited Zn^{2+} ion release; however, this effect is counterbalanced by the protective antioxidant components of the gum matrix, such as flavonoids and polyphenols. This dual behavior, mild oxidative induction coupled with strong biopolymer shielding, supports the suitability of G-ZnO for applications in wound healing, antimicrobial coatings, and tissue engineering, where controlled redox modulation is beneficial.

3.10. Molecular docking studies and mechanistic insights into antimicrobial activity

Molecular docking studies were conducted to elucidate the binding interactions between twelve bioactive antimicrobial compounds identified from PJ-Gum and four essential bacterial protein targets. Preliminary docking and affinity evaluations were performed using PyRx and CB-Dock2 platforms. Among the tested ligands, astilbin, epigallocatechin, and epicatechin demonstrated the strongest binding affinities (Supplementary Tables S6–S10). Of these, astilbin consistently exhibited the most favorable docking performance and was thus selected for detailed interaction analysis using Schrödinger Maestro 13.0. Astilbin displayed potent binding affinity toward topoisomerase II DNA gyrase from *Staphylococcus aureus* (PDB ID: 1AJ6), with docking scores ranging from −8.4 to −9.2 kcal/mol, indicating stable interactions within conserved active-site residues (Fig. 11A).

These interactions suggest that astilbin may potentiate antibiotic efficacy (e.g., novobiocin) by enhancing drug–target affinity, inducing conformational alterations, or promoting membrane disruption to facilitate intracellular drug uptake [60]. Against outer membrane penicillin acylase of *E. coli* (PDB ID: 1JX9), astilbin exhibited docking scores between −7.8 and − 8.1 kcal/mol (Fig. 11B). This enzyme plays a critical role in β-lactam antibiotic metabolism; thus, astilbin binding may disrupt protein processing, compromise membrane integrity, and interfere with metabolic pathways, thereby sensitizing bacterial cells.

For dihydrofolate reductase (DHFR) from *S. aureus* (PDB ID: 3SRW), astilbin achieved docking scores ranging from −9.5 to −10.2 kcal/mol

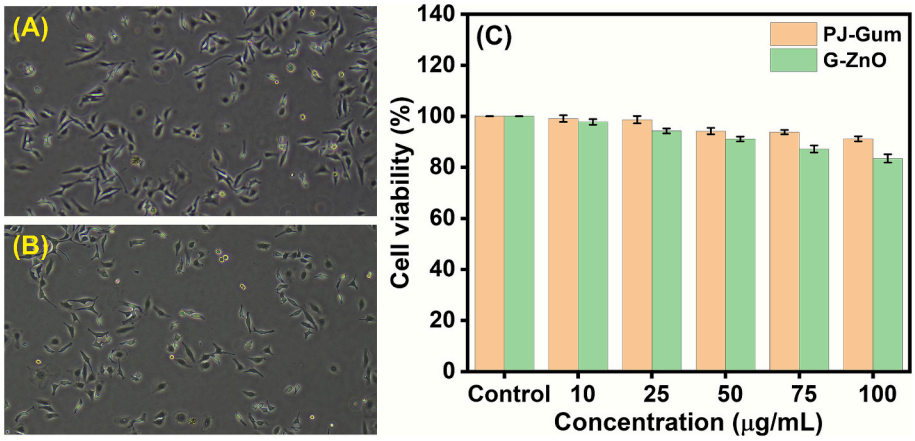

Fig. 10. MTT-based cell viability assay showing the comparative cytocompatibility of PJ-Gum and G-ZnO nanoparticles in HeLa cells after 24 h exposure. Both samples exhibited >80% viability across tested concentrations, confirming excellent biocompatibility.

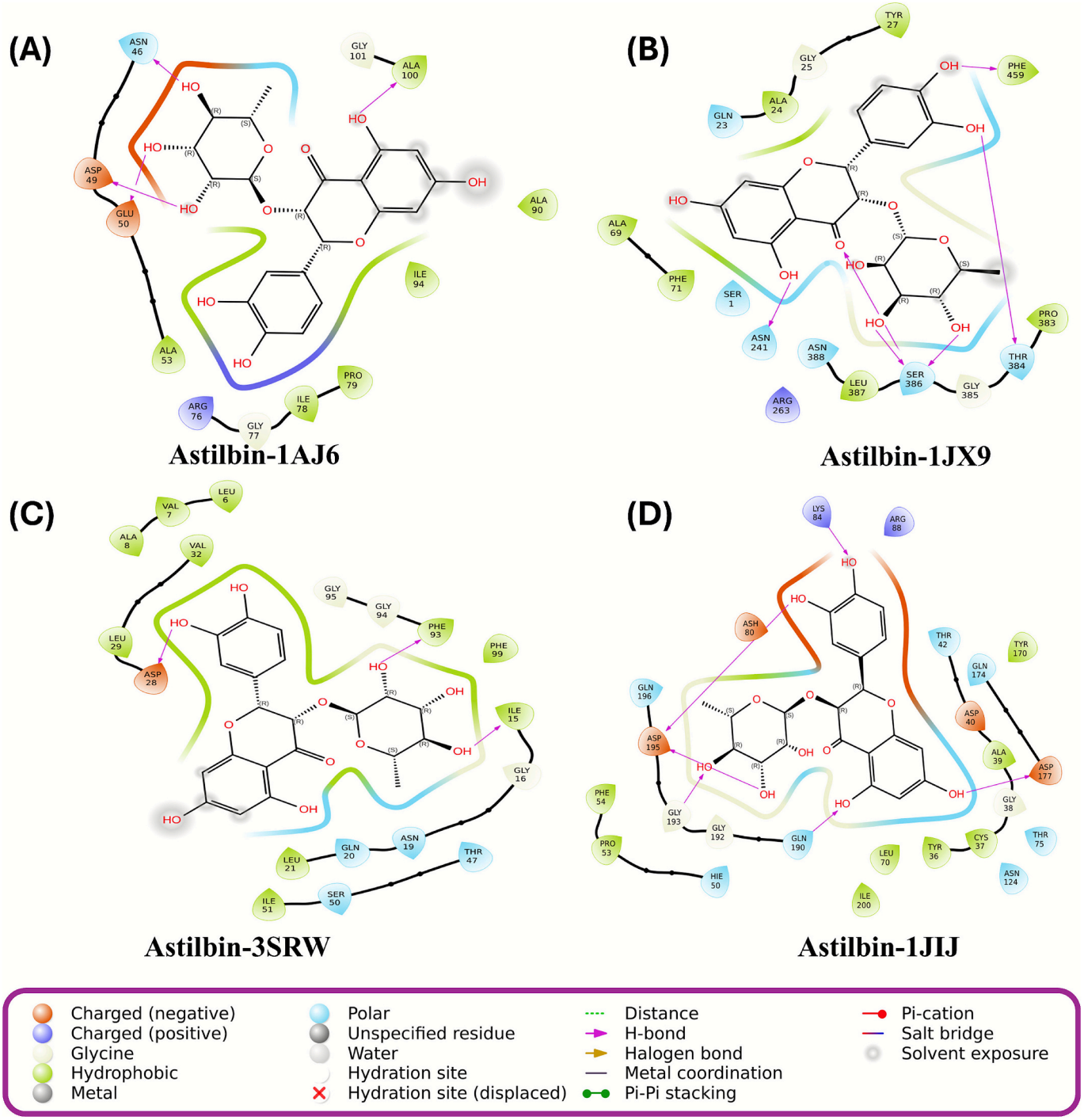

Fig. 11. Molecular interaction network showing binding of astilbin with four bacterial proteins: DNA gyrase (1JIJ), dihydropteroate synthase (1AJ6), and two membrane-associated proteins (1JX9, 3SRW).

(Fig. 11C). As DHFR is essential for nucleotide biosynthesis, strong astilbin binding indicates its potential to inhibit DNA replication and protein synthesis, leading to bacteriostatic or bactericidal effects.

Astilbin also showed robust affinity toward tyrosyl-tRNA synthetase from *E. coli* (PDB ID: 1JIJ), with docking scores of −9.4 to −9.6 kcal/mol (Fig. 11D). Interaction mapping revealed multiple π–π stacking and hydrogen bond interactions within the ATP-binding pocket, potentially impeding aminoacylation of tRNAˆTyr and obstructing protein synthesis at the translational level.

Notably, the incorporation of G-ZnO nanoparticles further amplified these antimicrobial effects. The nanoparticles are hypothesized to enhance bacterial membrane permeability, promote intracellular accumulation of astilbin, and induce ROS generation. This cascade leads to oxidative stress, protein denaturation, and DNA damage, resulting in synergistic bacterial inhibition and cell death. SEM analyses corroborated these findings. Untreated *E. coli* cells exhibited smooth, intact membranes (Fig. 12A), while those treated with G-ZnO showed severe morphological distortions, including membrane disruption, shrinkage, and deformation (Fig. 12B). High-magnification imaging revealed nanoparticles adhering to bacterial surfaces (Fig. 12C), consistent with ROS-mediated membrane perforation and cell lysis.

Additionally, treated cells displayed evidence of biofilm

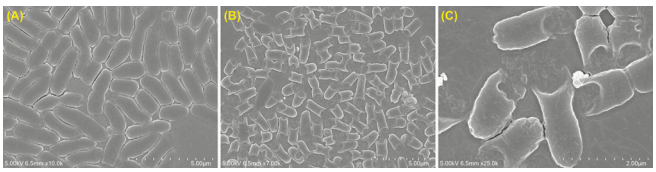

Fig. 12. SEM micrographs depicting bacterial morphological alterations: (A) untreated control cells; (B) G-ZnO NP-treated cells showing surface disruption; (C) Higher magnification revealing nanoparticle adherence, membrane perforation, and complete cell lysis.

disintegration, highlighting the nanoparticles' potential to eradicate both planktonic and sessile bacterial populations. These results identify astilbin as a key antimicrobial constituent of PJ-Gum and demonstrate that its synergistic interaction with ZnO nanoparticles enhances multi-targeted antibacterial efficacy. The dual mechanism, comprising biochemical inhibition of enzymatic pathways and physical disruption of membrane integrity, underscores the potential of PJ-Gum-derived nanocomposites for next-generation antimicrobial therapeutics.

3.11. In vitro antidiabetic and anti-inflammatory activities of PJ-gum and G-ZnO nanoparticles

The in vitro antidiabetic potential of PJ-Gum and G-ZnO NPs was evaluated through their inhibitory effects on pancreatic α-amylase activity using a fluorescence quenching assay. α-Amylase catalyzes the enzymatic hydrolysis of starch into glucose; hence, its inhibition is a key therapeutic target in managing postprandial hyperglycemia [61]. The native α-amylase enzyme (0.5 mg/mL) exhibited a strong intrinsic fluorescence emission peak at 340 nm, with an intensity of approximately 23,000–24,000 arbitrary units (a.u.) in the absence of inhibitors. Upon treatment with increasing concentrations of PJ-Gum and G-ZnO NPs (100–600 μg/mL), a dose-dependent decrease in fluorescence intensity was observed, suggesting effective enzyme–ligand binding and conformational disruption of the catalytic site.

As shown in Fig. 13A–B, G-ZnO demonstrated markedly stronger inhibitory effects, reducing fluorescence intensity to 5000–10,000 a.u., compared to PJ-Gum alone, which reduced it to 10,000–15,000 a.u. This enhanced inhibition may be attributed to the synergistic interaction between zinc oxide nanoparticles and the phytoconstituents of PJ-Gum, particularly astilbin, epicatechin gallate, and epicatechin—previously reported as potent α-amylase inhibitors [62]. The ligand-induced quenching and structural perturbation of α-amylase likely impair its enzymatic function, emphasizing the potential of G-ZnO as a dose-dependent antidiabetic agent.

In parallel, the anti-inflammatory activity of PJ-Gum and G-ZnO was assessed using the albumin denaturation assay, with egg albumin serving as the protein model and diclofenac sodium as the reference standard. Protein denaturation is a critical marker of inflammation, and its inhibition indicates the potential of a compound to mitigate inflammatory responses [63]. Both PJ-Gum and G-ZnO exhibited significant, concentration-dependent inhibition of protein denaturation in the range of 50–250 μg/mL (Fig. 13C). While both compounds were effective, G-ZnO displayed marginally higher inhibition percentages compared to PJ-Gum alone, reflecting the potential enhancement provided by ZnO nanoparticle incorporation. This suggests that the ZnO nanostructures interact with and stabilize protein conformations, preventing denaturation and thereby reducing inflammation. These findings underscore the dual bioactivity of G-ZnO, demonstrating both antidiabetic and anti-inflammatory potential. The superior performance of the nanoparticle formulation compared to the native gum suggests a synergistic effect between zinc oxide and phytochemical constituents. Nonetheless, further mechanistic and kinetic studies are warranted to delineate the precise molecular pathways and to optimize the bioactive concentration range for potential therapeutic applications.

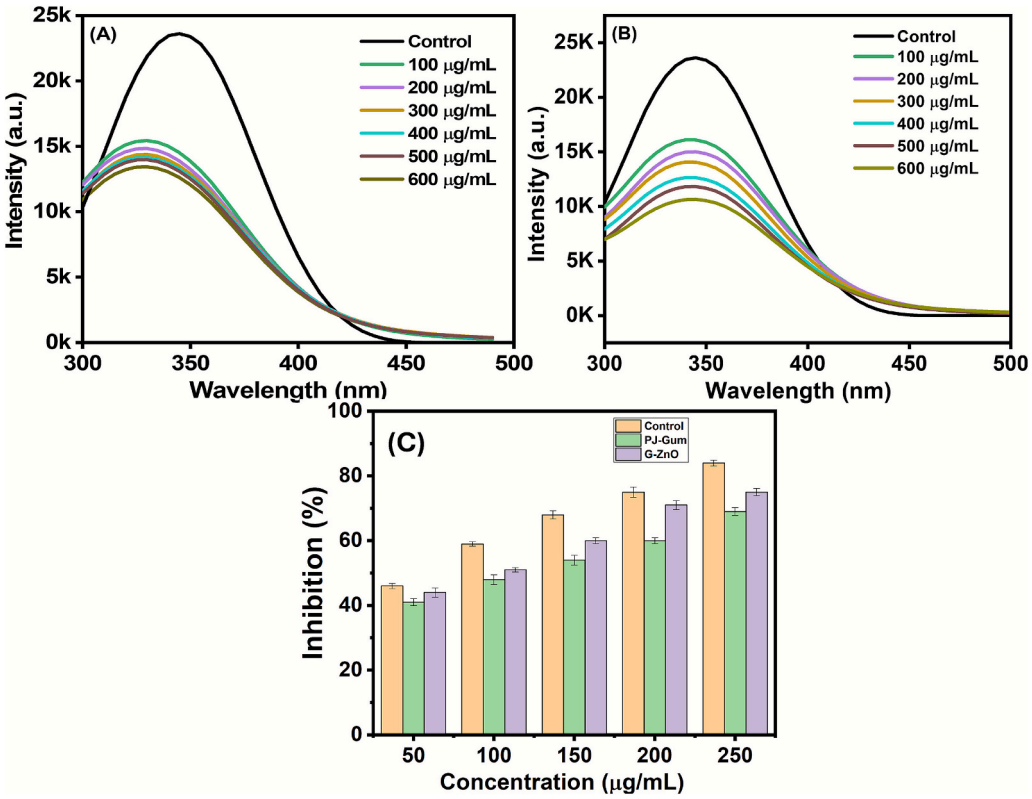

Fig. 13. In vitro antidiabetic and anti-inflammatory assays: (A) Fluorescence quenching of α-amylase by PJ-Gum; (B) Fluorescence quenching by G-ZnO;(C) Protein denaturation-based anti-inflammatory activity.

3.12. Proposed mechanism of antibacterial action of G-ZnO nanoparticles

The antibacterial efficacy of *Prosopis juliflora* gum-capped zinc oxide nanoparticles (G-ZnO NPs) arises from a multifaceted mechanism involving direct membrane disruption, ROS-mediated oxidative stress, and molecular interference with essential bacterial biomolecules [64,65]. A schematic overview of this proposed mechanism is illustrated in Fig. 14. The surface of G-ZnO, enriched with natural polymers and amphipathic flavonoids derived from *Prosopis juliflora* gum, promotes strong electrostatic and hydrophobic interactions with bacterial membranes. The biopolymeric matrix enhances nanoparticle adhesion through electrostatic attraction to negatively charged bacterial cell walls, while flavonoids, owing to their dual hydrophilic–lipophilic nature, integrate into the lipid bilayer, thereby compromising membrane integrity. This interaction leads to exopolysaccharide disruption, cell wall destabilization, and morphological alterations such as elongation, membrane blebbing, and disaggregation into smaller cellular [66]. These early events trigger mechanical and oxidative stress, impairing bacterial viability.

Concurrently, G-ZnO catalyze the formation of ROS at the cell membrane interface. The generation of superoxide anions (O_2^-), hydroxyl radicals ($^{\bullet}OH$), and hydrogen peroxide (H_2O_2) induces lipid peroxidation, protein oxidation, and membrane potential collapse, ultimately leading to cellular leakage and lysis [67]. The persistent ROS activity, coupled with penetration of bioactive gum-derived phytochemicals, results in nucleic acid degradation, enzyme inactivation, and metabolic disruption within bacterial cytoplasm. Molecular docking data support this proposed mechanism, revealing that astilbin—a major bioactive constituent of PJ-Gum — exhibits a strong binding affinity toward both membrane-associated proteins and intracellular bacterial targets, such as DNA gyrase and DHFR.

These interactions imply a dual-action mechanism: surface-level membrane perturbation and internal enzymatic inhibition, jointly contributing to bactericidal activity. The synergistic integration of phytochemical-rich gum with ZnO nanoparticles amplifies antibacterial potency by enhancing cellular uptake, ROS-mediated toxicity, and membrane perforation, collectively leading to irreversible cell death [68,69]. This multi-targeted mode of action positions G-ZnO NPs as a promising alternative to conventional antibiotics, particularly in the context of emerging antimicrobial resistances.

4. Conclusion

This study presents a sustainable, phytochemical and biopolymer-assisted approach for the green synthesis of G-ZnO using PJ-Gum, a natural carbohydrate polymer abundant in bioactive metabolites. Acting simultaneously as a reducing and stabilizing agent, PJ-Gum enabled the formation of highly stable, crystalline ZnO nanostructures with enhanced physicochemical and biological attributes. Comprehensive spectroscopic and structural characterizations verified effective biopolymer capping, which imparted colloidal stability, surface reactivity, and biocompatibility to the synthesized nanoparticles. The phytochemical diversity of the gum, elucidated through LC-QTOF-MS profiling, was central to the observed multifunctionality of G-ZnO. The nanoparticles exhibited broad-spectrum antimicrobial activity, driven by a multi-modal mechanism involving membrane disruption, ROS-mediated oxidative stress, and protein-target inhibition, as corroborated by molecular docking analyses. Beyond antimicrobial efficacy, G-ZnO demonstrated pronounced antioxidant, antidiabetic, and anti-inflammatory properties, highlighting their therapeutic potential in mitigating oxidative stress, microbial infections, and metabolic dysregulation. Importantly, the nanoparticles retained cytocompatibility across tested concentrations, underscoring the biosafety and biomedical promise of PJ-Gum as a natural nanocarrier. Collectively, these findings establish PJ-Gum–derived G-ZnO as a biologically active and eco-friendly nanoplatform that unites green chemistry principles with therapeutic efficacy. In summary, this work provides a compelling demonstration of how plant-derived carbohydrate polymers can be leveraged to engineer next-generation multifunctional nanomaterials. The G-ZnO system represents a promising candidate for advanced bioactive formulations, with potential applications in infection control, wound healing, and metabolic disease management. Future in vivo, pharmacokinetic, and tissue-targeting studies are warranted to accelerate the clinical translation of this biopolymer-mediated nanoplatform.

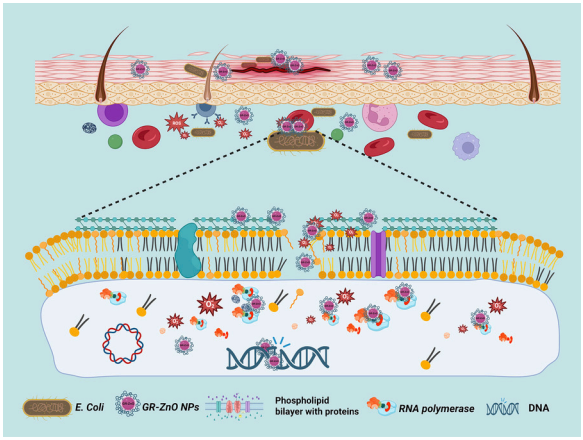

Fig. 14. Schematic representation of the proposed antibacterial mechanism of G-ZnO NPs, including membrane damage and oxidative stress pathways.

CRediT authorship contribution statement

Naveen Thanjavur: Writing – review & editing, Writing – original draft, Visualization, Validation, Software, Methodology, Investigation, Formal analysis, Data curation, Conceptualization. **Buddolla Anantha Lakshmi:** Formal analysis, Data curation. **Laxmi Bugude:** Visualization, Software, Methodology, Formal analysis, Data curation. **Kandaswamy Theyagarajan:** Visualization, Validation, Software, Methodology. **Young-Joon Kim:** Writing – review & editing, Supervision, Project administration, Funding acquisition, Conceptualization.

Declaration of competing interest

The authors declare that they have no known competing financial interests or personal relationships that could have appeared to influence the work reported in this paper.

Acknowledgments

This work was funded by the National Research Foundation of Korea (Grant number: NRF-2022R1F1A1074346 and RS-2024–00433166).

Appendix A. Supplementary data

Supplementary data to this article can be found online at https://doi.org/10.1016/j.ijbiomac.2025.149092.

Data availability

Data will be made available on request.

References

[1] P. Nagarajan, S. Kannan, A. Raj, L.R.P. Louis, A.B. Bazeer, R. Kaliaperumal, S. J. Patil, Future prospects in medicinal plant-derived drug development: unveiling opportunities and challenges, in: Biotechnology and Phytochemical Prospects in Drug Discovery, 2025, pp. 241–266.

[2] A. Singh, A review of various aspects of the ethnopharmacological, phytochemical, pharmacognostical, and clinical significance of selected medicinal plants, Asian J. Pharm. Technol. 12 (4) (2022), 349–0.
[3] P. Moliya, A. Singh, N. Singh, V. Kumar, A. Sohal, Insights into gastrointestinal manifestation of human immunodeficiency virus: a narrative review, World J. Virol. 14 (1) (2025) 99249.
[4] L.B. Martin, S. Kikuchi, M. Rejzek, C. Owen, J. Reed, A. Orme, A. Osbourn, Complete biosynthesis of the potent vaccine adjuvant QS-21, Nat. Chem. Biol. 20 (4) (2024) 493–502.
[5] N. Nurjannah, N. Noralina, R.S. Oktari, S.J. Wang, Elevated blood lead levels and associated risk factors among school children in a non-industrialized city in Indonesia, PLoS One 20 (10) (2025) e0332301.
[6] E. Breman, D. Ballesteros, E. Castillo-Lorenzo, C. Cockel, J. Dickie, A. Faruk, T. Ulian, Plant diversity conservation challenges and prospects—the perspective of botanic gardens and the millennium seed Bank, Plants 10 (11) (2021) 2371.
[7] H. Munir, M. Bilal, M.I. Khan, H.M. Iqbal, Gums-Based Bionanostructures for Medical Applications, in: Polysaccharides: Properties and Applications, 2021, pp. 385–398.
[8] R.B. Malabadi, K.P. Kolkar, R.K. Chalannavar, Natural plant gum exudates and mucilage: pharmaceutical updates, Int. J. Innov. Sci. Res. Rev. 3 (10) (2021) 1897–1912.
[9] R.V. Asase, T.V. Glukhareva, Production and application of xanthan gum—prospects in the dairy and plant-based milk food industry: a review, Food Sci. Biotechnol. 33 (4) (2024) 749–767.
[10] S. Barak, D. Mudgil, S. Taneja, Exudate gums: chemistry, properties and food applications–a review, J. Sci. Food Agric. 100 (7) (2020) 2828–2835.
[11] G. Joshi, K.S. Yadav, Applications of bioresins and biopolymers derived from natural resources as composites in drug delivery, in: Green Sustainable Process for Chemical and Environmental Engineering and Science, Elsevier, 2023, pp. 21–34.
[12] D.A. da Silva, G.C.M. Aires, Applications in the food industry, in: Innovation in the food sector through the valorization of food and agro-food by-products, 2021, p. 233.
[13] R.K. Upadhyay, Plant origin anti-inflammatory and immunomodulatory agents and their mechanism of action: a review, Int. J. Green Pharm. 19 (01) (2025).
[14] M. Irfan, F. Nasir, M. Naveed, S. Javed, Z. Yousaf, S. Shafiq, H. Munir, Unlocking the potential of plant gums: bioinformatics-driven insights into green synthesis and applications of metal-based nanoparticles, Int. J. Biol. Macromol. 308 (2025) 142584.
[15] S. Ihsan, H. Munir, Z. Meng, M. Tayyab, N. Zeeshan, A. Rehman, M. Irfan, Tragacanth gum-based copper oxide nanoparticles: comprehensive characterization, antibiofilm, antimicrobial and photocatalytic potentials, Int. J. Biol. Macromol. 268 (2024) 131600.
[16] I.E. Dávila-Rangel, A.V. Charles-Rodríguez, J.C. López-Romero, M.L. Flores-López, Plants from arid and semi-arid zones of Mexico used to treat respiratory diseases: A review, Plants 13 (6) (2024) 792.
[17] R.K. Upadhyay, Anti-inflammatory activity of plant-derived natural bio-organic ingredients: a review, Int. J. Green Pharm. 19 (02) (2025).
[18] R.A. Prasath, R. Mohanraj, In situ bioaccumulation of metals by *Prosopis juliflora* and its detoxification potential at the metal contaminated sites, Sci. Total Environ. 951 (2024) 175715.
[19] A. Esmeeta, S. Adhikary, V. Dharshnaa, P. Swarnamughi, Z.U. Maqsummiya, A. Banerjee, A.K. Duttaroy, Plant-derived bioactive compounds in colon cancer treatment: an updated review, Biomed. Pharmacother. 153 (2022) 113384.
[20] D. Mudgil, S. Barak, Mesquite gum (Prosopis gum): structure, properties & applications-A review, Int. J. Biol. Macromol. 159 (2020) 1094–1102.
[21] I.A. Saleh, A. BiBi, S. Bibi, M. Abu-Dieyeh, M.A. Al-Ghouti, Waste-to-value: guidelines for the potential applications of Prosopis juliflora, Bioresour. Technol. Rep. 24 (2023) 101678.
[22] K. Katragunta, B. Siva, N. Kondepudi, P.R. Vadaparthi, N.R. Rao, A.K. Tiwari, K. S. Babu, Estimation of boswellic acids in herbal formulations containing Boswellia serrata extract and comprehensive characterization of secondary metabolites using UPLC-Q-Tof-MSe, J. Pharm. Anal. 9 (6) (2019) 414–422.
[23] M. Bilal, H. Munir, M.I. Khan, M. Khurshid, T. Rasheed, K. Rizwan, H.M. Iqbal, Gums-based engineered bio-nanostructures for greening the 21st-century biotechnological settings, Crit. Rev. Food Sci. Nutr. 62 (14) (2022) 3913–3929.
[24] J. Jiang, J. Pi, J. Cai, The advancing of zinc oxide nanoparticles for biomedical applications, Bioinorg. Chem. Appl. 2018 (1) (2018) 1062562.
[25] K.S. Siddiqi, A. Ur Rahman, N. Tajuddin, A. Husen, Properties of zinc oxide nanoparticles and their activity against microbes, Nanoscale Res. Lett. 13 (2018) 1–13.
[26] C. Mahendra, M.N. Chandra, M. Murali, M.R. Abhilash, S.B. Singh, S. Satish, M. S. Sudarshana, Phyto-fabricated ZnO nanoparticles from Canthium dicoccum (L.) for antimicrobial, anti-tuberculosis and antioxidant activity, Process Biochem. 89 (2020) 220–226.
[27] N. Asif, M. Amir, T. Fatma, Recent advances in the synthesis, characterization and biomedical applications of zinc oxide nanoparticles, Bioprocess Biosyst. Eng. 46 (10) (2023) 1377–1398. Springer Science+Business Media.
[28] U. Singhal, R. Pendurthi, M. Khanuja, Prunus: A natural source for synthesis of zinc oxide nanoparticles towards photocatalytic and antibacterial applications, Elsevier BV 28 (2020) 261–265.
[29] M. Pradeep, D. Kruszka, P. Kachlicki, D. Mondal, G. Franklin, Uncovering the phytochemical basis and the mechanism of plant extract-mediated eco-friendly synthesis of silver nanoparticles using ultra-performance liquid chromatography coupled with a photodiode array and high-resolution mass spectrometry, ACS Sustain. Chem. Eng. 10 (1) (2021) 562–571.
[30] Z. Gu, Y. Guo, X. Mao, M. Qi, B. Ge, Green synthesis of nanomaterials mediated by herbal medicine: mechanism, characterization, and application prospects, Nat. Prod. Commun. 20 (8) (2025) 1934578X251365007.
[31] A.B.S. de Lemos, G. Chaves, P.P.C. Ribeiro, K.S.F. da Silva Chaves Damasceno, Prosopis juliflora: nutritional value, bioactive activity, and potential application in human nutrition, J. Sci. Food Agric. 103 (12) (2023) 5659–5666.
[32] I. Blaženović, T. Kind, J. Ji, O. Fiehn, Software tools and approaches for compound identification of LC-MS/MS data in metabolomics, Metabolites 8 (2) (2018) 31.
[33] K.I. Tapfuma, L. Mekuto, M.M. Makatini, V. Mavumengwana, The LC-QTOF-MS/MS analysis data of detected metabolites from the crude extract of Datura stramonium leaves, Data Brief 25 (2019) 104094.
[34] M.S. Almuhayawi, M.H. Alruhaili, M.K. Soliman, M.K. Tarabulsi, R.A. Ashy, A. A. Saddiq, S.S. Salem, Investigating the in vitro antibacterial, antibiofilm, antioxidant, anticancer and antiviral activities of zinc oxide nanoparticles biofabricated from Cassia javanica, PLoS One 19 (10) (2024) e0310927.
[35] O.J. Avwioroko, A.A. Anigboro, C.A. Otuechere, F.O. Atanu, O.F. Dairo, T. T. Oyetunde, N.J. Tonukari, A-amylase inhibition, anti-glycation property and characterization of the binding interaction of citric acid with α-amylase using multiple spectroscopic, kinetics and molecular docking approaches, J. Mol. Liq. 360 (2022) 119454.
[36] M. Singh, A. Dhanwal, A. Verma, L. Augustin, N. Kumari, S. Chakraborti, R.J. Dey, Discovery of potent antimycobacterial agents targeting lumazine synthase (RibH) of mycobacterium tuberculosis, Sci. Rep. 14 (1) (2024) 12170.
[37] A. Kuplińska, K. Rząd, J. Stefaniak-Skorupa, K. Kozłowska-Tylingo, M. Wojciechowski, S. Milewski, I. Gabriel, Targeting Candida albicans O-acetyl-L-homoserine sulfhydrylase (Met15p) in antifungal treatment, Sci. Rep. 14 (1) (2024) 28188.
[38] J.M. Han, I. Yun, K.M. Yang, H.S. Kim, Y.Y. Kim, W. Jeong, I. Hwang, Ethanol extract from Astilbe chinensis inflorescence suppresses inflammation in macrophages and growth of oral pathogenic bacteria, PLoS One 19 (7) (2024) e0306543.
[39] J. Wang, N. Battini, M.F. Ansari, C.H. Zhou, Synthesis and biological evaluation of quinazolonethiazoles as new potential conquerors towards Pseudomonas aeruginosa, Chin. J. Chem. 39 (5) (2021) 1093–1103.
[40] V.N. Lima, C.D. Oliveira-Tintino, E.S. Santos, L.P. Morais, S.R. Tintino, T.S. Freitas, H.D. Coutinho, Antimicrobial and enhancement of the antibiotic activity by phenolic compounds: gallic acid, caffeic acid and pyrogallol, Microb. Pathog. 99 (2016) 56–61.
[41] M.A. Morsy, E.M. Ali, M. Kandeel, K.N. Venugopala, A.B. Nair, K. Greish, M. El-Daly, Screening and molecular docking of novel benzothiazole derivatives as potential antimicrobial agents, Antibiotics 9 (5) (2020) 221.
[42] D. Buchmann, N. Schultze, J. Borchardt, I. Böttcher, K. Schaufler, S. Guenther, Synergistic antimicrobial activities of epigallocatechin gallate, myricetin, daidzein, gallic acid, epicatechin, 3-hydroxy-6-methoxyflavone and genistein combined with antibiotics against ESKAPE pathogens, J. Appl. Microbiol. 132 (2) (2022) 949–963.
[43] S. Masri, N. Mohd, N.H. Abu Kasim, M. Razali, Mechanistic insight into the antioxidant and antimicrobial activities of palm oil-derived biomaterials: implications for dental and therapeutic applications, Int. J. Mol. Sci. 26 (14) (2025) 6975.
[44] G. de Araújo Delmondes, M.J.P. Lopes, I.M. Araújo, A. de Sousa Borges, P. R. Batista, H.D.M. Coutinho, M.R. Kerntopf, Possible mechanisms involved in the neuroprotective effect of trans, trans-farnesol on pilocarpine-induced seizures in mice, Chem. Biol. Interact. 365 (2022) 110059.
[45] R. Glenz, A. Kaiping, D. Göpfert, H. Weber, B. Lambour, M. Sylvester, F. Waller, The major plant sphingolipid long chain base phytosphingosine inhibits growth of bacterial and fungal plant pathogens, Sci. Rep. 12 (1) (2022) 1081.
[46] C. Hamper, H.J. Campbell, R. Luo, M. Murphy, P. Gleason, T. Smith, R. Jagan, Selective synthesis of deuterated cis-and trans-isohumulones and trans-isohumulinones, Synthesis 56 (20) (2024) 3206–3214.
[47] E. Rahayu, V. Wonoputri, T.W. Samadhi, Plant extract-assisted biosynthesis of zinc oxide nanoparticles and their antibacterial application, In IOP Conference Series: Mater. Sci. Eng. 823 (1) (2020) 012036.
[48] D. Cao, S. Gong, X. Shu, D. Zhu, S. Liang, Preparation of ZnO nanoparticles with high dispersibility based on oriented attachment (OA) process, Nanoscale Res. Lett. 14 (1) (2019) 210.
[49] G. Topcu, A.M. Al Hindawi, C. Feng, D. Spence, B. Sitorus, H. Liu, S. Yang, Precision engineering of nano-assemblies in superfluid helium by the use of van der Waals forces, Commun. Chem. 7 (1) (2024) 125.
[50] M.H. Shibraen, O.M. Ibrahim, R.A. Asad, S. Yang, M.R. El-Aassar, Interpenetration of metal cations into polyelectrolyte-multilayer-films via layer-by-layer assembly: selective antibacterial functionality of cationic guar gum/polyacrylic acid-ag+ nanofilm against resistant *E. Coli*, Colloids Surf. A Physicochem. Eng. Asp. 610 (2021) 125921.
[51] F. Rincón-Acosta, M.E. Félix López, E. Antonio Hurtado, R. Guerrero-Castillo, O. Beltrán, Surfactant properties and emulsifying activity of the gum exudate of *Prosopis juliflora* (Sw.) DC 40 (2) (2023) e234013.
[52] M. Irfan, S. Bagherpour, H. Munir, L. Perez-Garcia, T.F. Abelha, A. Afroz, U. Rashid, GC–MS metabolomics profile of methanol extract of *Acacia modesta* gum and gum-assisted fabrication and characterization of gold nanoparticles through green synthesis approach, Int. J. Biol. Macromol. 252 (2023) 126215.
[53] M. Zahra, H. Abrahamse, B.P. George, Flavonoids: antioxidant powerhouses and their role in nanomedicine, Antioxidants 13 (8) (2024) 922.
[54] S.M. Karimi, M. Bayat, R. Rahimi, Plant-derived natural medicines for the management of osteoporosis: A comprehensive review of clinical trials, J. Tradit. Complement. Med. 14 (1) (2024) 1–18.

[55] M. Nilavukkarasi, S. Vijayakumar, S. Prathipkumar, Capparis zeylanica mediated bio-synthesized ZnO nanoparticles as antimicrobial, photocatalytic and anti-cancer applications, Mater. Sci. Energy Technol. 3 (2020) 335–343.
[56] S. Shafqat, H. Munir, J. Najeeb, K. Naseem, M. Irfan, Fabrication of multifaceted alpha-alumina nanoparticles: exploring bioactive and photocatalytic properties, BioNanoScience 15 (2) (2025) 237.
[57] W. Xu, Z. Lin, C. Cortez-Jugo, G.G. Qiao, F. Caruso, Antimicrobial phenolic materials: from assembly to function, Angew. Chem. Int. Ed. 64 (2025) e202423654.
[58] C.U. Athira, K. Krishnakumar, Antioxidant, anticancer, and anti-inflammatory potential of carotenoids produced by green microalga *Asterarcys quadricellulare* (K. Behre) E. Hegewald & AWF Schmidt, Pharmacol. Res. Nat. Prod. 7 (2025) 100190.
[59] M.W. Gielisch, D.G. Thiem, U. Ritz, C. Bösing, B. Al-Nawas, P.W. Kämmerer, Assessing cytotoxicity: A comparative analysis of biodegradable and conventional 3D-printing materials post-steam sterilization for surgical guides, Biomed. Mater. 20 (1) (2024) 015001.
[60] J.M. Han, I. Yun, K.M. Yang, H.S. Kim, Y.Y. Kim, W. Jeong, I. Hwang, Ethanol extract from Astilbe chinensis inflorescence suppresses inflammation in macrophages and growth of oral pathogenic bacteria, PLoS One 19 (7) (2024) e0306543.
[61] V. Varadharaj, A. Ramaswamy, R. Sakthivel, R. Subbaiya, H. Barabadi, M. Chandrasekaran, M. Saravanan, Antidiabetic and antioxidant activity of green synthesized starch nanoparticles: an in vitro study, J. Clust. Sci. 31 (2020) 1257–1266.
[62] K. Eawsakul, T. Ongtanasup, N. Ngamdokmai, K. Bunluepuech, Alpha-glucosidase inhibitory activities of astilbin contained in Bauhinia strychnifolia Craib. Stems: an investigation by in silico and in vitro studies, BMC complementary medicine and therapies 23 (1) (2023) 25.
[63] K. Ramasubbu, S. Padmanabhan, K.A. Al-Ghanim, M. Nicoletti, M. Govindarajan, N. Sachivkina, V.D. Rajeswari, Green synthesis of copper oxide nanoparticles using Sesbania grandiflora leaf extract and their evaluation of anti-diabetic, cytotoxic, anti-microbial, and anti-inflammatory properties in an in-vitro approach, Fermentation 9 (4) (2023) 332.
[64] J. Park, T.H. Bae, S.Y. Kim, S. Park, Y. Choi, M. Tanaka, J. Choi, Photocatalytic effect of gold-zinc oxide composite nanostructures for the selective and controlled killing of antibiotic-resistant bacteria and the removal of resistant bacterial biofilms from the body, Nano Convergence 12 (1) (2025) 1–21.
[65] N. Thanjavur, A. Buddolla, L. Bugude, V. Buddolla, Y.J. Kim, Ultrasonic nanotechnology for the effective management of *Staphylococcus aureus* skin infections: an update, Nanoscale 16 (2024) 16329–16343.
[66] A. Raghav, S. Kaur, G. Setia, S. Kumar, Nanomaterials induced cell disruption: An insight into mechanism, in: Biogenic Nanomaterials for Environmental Sustainability: Principles, Practices, and Opportunities, Springer International Publishing, Cham, 2024, pp. 227–249.
[67] N. Thanjavur, R. Sangubotla, B.A. Lakshmi, R. Rayi, C.D. Mekala, A.S. Reddy, B. Viswanath, Evaluating the antimicrobial and apoptogenic properties of bacteriocin (nisin) produced by Lactococcus lactis, Process Biochem. 122 (2022) 76–86.
[68] Z.X. Zhong, S. Zhou, Y.J. Liang, Y.Y. Wei, Y. Li, T.F. Long, J. Sun, Natural flavonoids disrupt bacterial iron homeostasis to potentiate colistin efficacy, Sci. Adv. 9 (23) (2023) eadg4205.
[69] R. Zhang, Y. Liu, S. Wang, J. Kang, Y. Song, D. Yin, J. Duan, Anti-bacteria, anti-biofilm, and anti-virulence activity of the synthetic compound MTEBT-3 against carbapenem-resistant Klebsiella pneumoniae strains ST3984, Microb. Pathog. 197 (2024) 107068.